UNIVERSITÀ DI PISA

CORSO DI LAUREA MAGISTRALE IN INGEGNERIA
DELLE TELECOMUNICAZIONI

Tesi di Laurea Magistrale

INTERNAL CALIBRATION FOR HIGH-BEAMWIDTH, HIGH-BANDWIDTH UAV-SAR SYSTEMS

Relatrice:
Prof. Maria Sabrina Greco
Relatori esterni:
Dr. Markus Peichl
Philipp Brücker

Candidato:
Alessio Ulivi

ANNO ACCADEMICO 2023-2024

CONTENTS

LIST OF ACRONYMS

DOA: Direction of Arrival
EM: Electromagnetic
ISAR: Inverse Synthetic Aperture Radar
PRI: Pulse Repetition Interval
PSF: Point Spread Function
RCS: Radar Cross Section
RF: Radio Frequency
SAR: Synthetic Aperture Radar
UAV: Unmanned Aerial Vehicles

ABSTRACT

The proliferation of unmanned aerial vehicles (UAV) in recent years has piqued the interest of the scientific community, due to the ability to equip them with complex and advanced synthetic aperture radar (SAR) systems. UAV-SAR systems bring many advantages to the users, but they also come with new challenges. Among them, there is the problem of finding an effective and validated calibration procedure that can yield the radiometrically-accurate image of the scene. The thesis firstly questions about the applicability of existing internal calibration methods, developed with classical (air- and spaceborne) SAR systems in mind, to UAV-SAR systems. The document goes on to elucidate and emphasize the significant differences that set apart air- and spaceborne systems from UAV-SAR systems, with simulated results backing up the claims. Then, a state-of-the-art internal calibration procedure designed for an airborne SAR system undergoes testing and analysis. Finally, theoretical progress is presented through comprehensive problem analysis, and innovative solutions are suggested.

INTRODUCTION

Synthetic aperture radar (SAR) systems exist ever since the 1950s [1], after which the world soon realized the usefulness of this technology for many scientific and practical applications. The ability to observe the earth with great resolution from a large distance opened up new possibilities for the scientific community. Data acquired with airborne and, especially, spaceborne SAR systems provided consistent observation of physical quantities, thus enabling time-series of large scale natural phenomena [2]. However, in the last two or so decades, interest has also emerged for a more localized form of radar imaging [3].

In recent years, unmanned aerial vehicles (UAV) [4], commonly referred to as drones, have seen a great development and, nowadays, the technology is well-established. The commercial availability of drones, with particular focus on the multi-copter type of UAVs, sprouted the interest of institutes and universities, which started experimenting with them. The conjunction of drones and radar systems is now giving birth to a new kind of SAR system, whose presence will open up new opportunities regarding acquisition geometries and enable high-bandwidth, high-beamwidth SAR systems. Research in the field of UAV-SAR systems is now being carried on by many research groups from institutes and companies, both in terms of technology development [5]-[10] and its applicability [11], [12].

The growing interest in this technology is justified by the great advantages that a lightweight, small SAR system brings to the users. Starting from the aerodynamics point-of-view, UAVs are the most flexible vehicle type that could be deployed in the air. Their high maneuverability allows them to change flight direction in mid-air without straying from the expected trajectory. Furthermore, the on-board flight controller can be pre-programmed with any trajectory, which will then be automatically followed without human intervention. From a SAR point-of-view, the UAV-SAR system allows to perform most of the applications that are currently being done with air- and spaceborne systems. However, the greater flexibility in flight paths means a better image resolution, for instance when using circular trajectories [13, Sec. 7.4], and the revisit time is arbitrarily decided, since the deployment is as immediate as placing the drone on the ground and turning it on. Lastly but most importantly, the overall costs of using a UAV as the platform hosting the radar are significantly lower with respect to the costs of getting a plane off the ground or launching a satellite. A more in-depth analysis of UAV-SAR systems, alongside some examples of applications, is given in [14] and references therein.

As briefly discussed, the introduction of UAVs in the field of radar imaging brought quite some advantages, but it also brought new challenges. The same problems faced in the development of the other SAR systems, for which solutions are already present in literature and implemented in the actual systems, need to be faced again in the case of UAV-SAR systems. The completely different scenarios, technological requirements and scientific goals, that shape the development of these new systems, shatter the underlying assumptions required by the aforementioned solutions found in literature. Among the various new challenges, one of the most relevant for the scientific community is the problem of calibrating the SAR system.

Any system that performs a measure of a physical quantity, can only output data that is related to the actual quantity. The relationship that holds between data and physical quantity depends on various things, but in general one cannot take the output data as is and consider it to be the actual physical quantity. Therefore, a calibration procedure is needed, in order to obtain the physical quantity from the data. In other words, the calibration aims to remove any undesired effects introduced by the system in the measured data. In the case of a SAR system, the measured quantity is the radiometric or radar backscatter data of the observed scene [15, Sec. II], which is related to the equivalent radar cross section (RCS) of each target in the scene [16]. The existence of a calibration procedure that can transform the observed data into radiometric measurements is very important in many scientific applications [17], [18]. Ideally, after calibrating the SAR images, each pixel value would correspond to the equivalent RCS of the target in that pixel, which can then be related to other geophysical quantities of interest. Moreover, another important aspect of calibration is the removal of distortions caused by the systems transfer function from the image, that prevent the direct comparison of different values inside the same image or across different images.

UAV-SAR systems also need to be calibrated, but the scenarios they face complicate the problem even further. The acquisition geometry of drones is such that the platform is very close to the targets. Compared to planes and satellites, which are tens or hundreds of kilometers away from the ground, drones are only tens of meters above the ground. Furthermore, different trajectories can be exploited and new science requisites are being proposed, like for instance the use of very high-bandwidth signals in conjunction with low operative frequencies [19]. The combination of all these things make the already known effects more impacting on the image and create problems that are investigated in detail in this thesis.

In light of these huge differences with respect to the other well-known technologies, more research must be done on UAV-SAR systems. This is the reason why in this thesis the problem of calibration is tackled in detail, in order to discover whether the calibration procedures present in literature can still be applied to these systems. Firstly, in the following chapters some common-ground definitions about calibration and SAR image formation are given. Afterwards, it is necessary to introduce the simulator, specially created to cope with this new kind of scenarios. The simulated results will highlight the kind of output images to be expected from UAV-SAR systems and the problem that affects them. Proceeding to the core of the work, the applicability of a state-of-the-art airborne SAR calibration procedure is investigated, and the simulated results are presented and analyzed. Finally, a more detailed theoretical treatment of the problem is advanced and other solutions are proposed, speculating what could be achieved next.

Chapter 1

THE CALIBRATION PROCEDURE IN SAR SYSTEMS

To this day, SAR images are also being used in their rawest form, i.e. right after image processing, to perform data analysis and extract useful information about the earth [20, Ch. 4]. This kind of qualitative analyses of SAR images requires much less processing steps and still allows to get important results [11], [21], mainly thanks to the human intervention in the processing chain. In fact, the human brain is very capable when it comes to blanking out the undesired effects present in the data, only considering the useful parts and even trying to adjusting the distorted portions of the image. Nonetheless, in order to obtain reliable high-level products through automated algorithms, the provided data must represent a physical quantity.

This can only be achieved by performing a radiometric calibration of SAR images. The radiometric calibration procedure processes SAR data, either before or after focusing the image, in such a way that the final result is a measurement of the RCSs of the scene, whose accuracy depends on the applied method. Depending on the application, the scientific requirements for calibration are different [15, Tab. I], but in general they are very stringent and it is important for the calibration algorithms to be characterized and well understood. Having very accurate power levels is key for all the applications using the calibrated SAR images. Every processing step that leads to higher-level products adds its own errors and amplifies the already present offsets. Therefore, it is mandatory to obtain accurate images from the very beginning.

1.1 How calibration is performed

The scientific requisites on data accuracy pose a great burden on the design of a calibration procedure, which nevertheless achieves the required standards by means of two mandatory steps: the internal and external calibrations [15]. The former relies only on measurements and predictions made by the system itself, meanwhile the second method validates and further refines the compensation performed by the first.

The signal generated by the radar undergoes a lot of transformations, from simple amplifications to the very complex conversion into an electromagnetic (EM) wave and vice versa. The resulting data and the processed SAR image are therefore affected by many terms, as it will be analyzed in next chapter. Calibration procedures, beginning with internal calibration, effectively address the distortions introduced by these terms. As the name may suggest, internal calibration refers to a process that is contained within the system itself. The main role of this process is to remove the distortions in the targets' responses, through the measurements of the terms that influence the received signal, and restore the original image as much as possible.

The effectiveness of internal calibration is determined by two aspects: the applied algorithm and, mainly, how reliable the measurements are. Among the many factors that need to be compensated, the main source of uncertainty is the antenna gain [15], as it is not easy to measure exactly once mounted on the platform and, most importantly, it is very hard to compensate. The antenna gain is a function of frequency and looking direction, therefore its influence on the signal is very complex and depends on the particular acquisition geometry. This problem, alongside the effectiveness of the applied algorithm, will be discussed in great detail throughout this thesis.

Ideally, just by applying internal calibration alone, the resulting image would be expressed in terms of the equivalent RCS of the scene. Unfortunately, the great uncertainty that comes with every measurement and the imperfect calibration methods undermine the overall accuracy of the calibration. This is where external calibration comes into play. The purpose of this second step is to introduce external sources of calibration, that should overcome the limitations of internal measurements. The external sources are well-known reference targets, characterized in terms of their RCSs, placed strategically in the scene. After SAR processing and internal calibration, the image should clearly show these high-reflectivity targets in their respective locations. Comparing the actual power values with the expected values of RCS, it is possible to adjust the image amplitude and finally get the RCS map of the entire scene with the appropriate level of accuracy.

Summing up, internal calibration has the very important task of reducing the distortions in the image, possibly even for the phase, meanwhile external calibration adjust the power level using a ground-truth reference, as expected by the definition of calibration. The two steps are complementary and the whole calibration procedure cannot be composed of just either one of the two. Without external references, the accuracy of the internal measurements cannot be assessed and compensated, hence it cannot be trusted. Meanwhile, external calibration alone cannot take care of the great distortions introduced by the system.

1.2 Calibration in SAR system

In air- and spaceborne systems, internal calibration usually compensates for the distortions introduced by the radar's components and some propagation effects [22], [23], [24], offloading to external calibration the compensation for the antenna gain and every other imperfection of the system model. For example, the study in [25] proposes a method for external calibration that compensates for direction-dependent distortions, such as antenna gain. Therefore, internal calibration for these systems is mostly performed in the radar front-end hardware and is localized, not taking into account the full SAR signal model. Meanwhile, external calibration relies on known reference targets in the scene, which can only give limited information about the whole acquired data. In fact, especially in regard to the antenna gain, the reference targets only return data from their direction and location in the scene. However, in SAR systems with small-beamwidth antennas, small relative bandwidth and fixed trajectories, this kind of procedure is able to meet the scientific requirements for radiometric calibration.

On the other hand, UAV-SAR systems generally fly closer to the observed scene and push for higher resolutions, employing high-bandwidth transmitted signals. In addition, drones have weight limitations regarding the payload, with the antenna being the heaviest of the components. Combined with the fact that low frequencies are also of interest for some applications, UAV-SAR systems mount electrically small antennas, which in turn have an high beamwidth. These characteristics determine the need for a new approach to SAR calibration, one that considers the three-dimensional acquisition geometry, comprising the platform's rotation, and the full antenna gain as a function of frequency and looking direction. Hence, internal calibration in this case is not limited to phase and amplitude corrections of internal system components, like amplifiers and such, but it must also compensate for the more complex distortions introduced in the signal propagation chain. The procedure should then be able to integrate everything in a powerful signal processing algorithm that makes full use of the signal model described in Ch. 2.

In the early stages of developing drone-borne SAR systems, calibration procedures were not used at all. Even now, this remains the case due to the absence of a validated method. Furthermore, the combination of high-beamwidth antennas, high-bandwidth signals, very low flight altitudes, and arbitrary trajectories results in greater distortions in the system's response function. This raises doubts about the applicability of existing methods. Therefore, the main goal of this thesis is to evaluate the calibration procedures found in literature, with a focus on internal calibration, and establish whether they are applicable to UAV-SAR systems and to what extent.

Chapter 2

THE RECEIVED SIGNAL MODEL

In the field of SAR imaging, the signal model is often a very simplified description of what the radar actually receives. In air- and spaceborne applications, there are a number of assumptions that can be made, with the most important being the fixed trajectory of the platform. Particularly for satellites, and also applicable to numerous airborne SAR acquisition methods, the trajectory of the platform is a straight line motion that runs parallel to the Earth's surface. Therefore, the signal model can be elaborated with a very case-specific mathematical treatment [26] and the resulting SAR algorithms are only applicable under numerous assumptions. This significantly streamlines the processing algorithms in terms of both complexity and computational demand. Furthermore, the reduced applicability of the model is not a practical limitation, since the vast majority of SAR systems are designed to work in these conditions.

However, the case of UAV-SAR systems is very different. The close distance of the acquisition geometry and the arbitrariness of the trajectory require a more generalized approach to the problem. The following sections set the fundamental definitions about the scenario, the geometry and the model used to describe the target, then proceed to give a more detailed model of the received signal. The model presented here doesn't restrict the treatment to any specific scenario and it's the same signal model also used for inverse SAR (ISAR) imaging; a detailed derivation can be found in [27].

2.1 Scenario definition

In a generic SAR scenario, there are fundamentally two actors: the platform and the target. The platform, in a more general sense, could be composed of a multitude of transmitters and receivers independently moving in space, but in the scope of this thesis, the interest is on monostatic radars. Hence, there is only one physical platform that transmits and receives the signals, which can nonetheless move and rotate. The target is instead considered static with respect to the global reference system. A more detailed description of the target will be given shortly after, so for now consider a point of interest in the scene that could represent a point-like target.

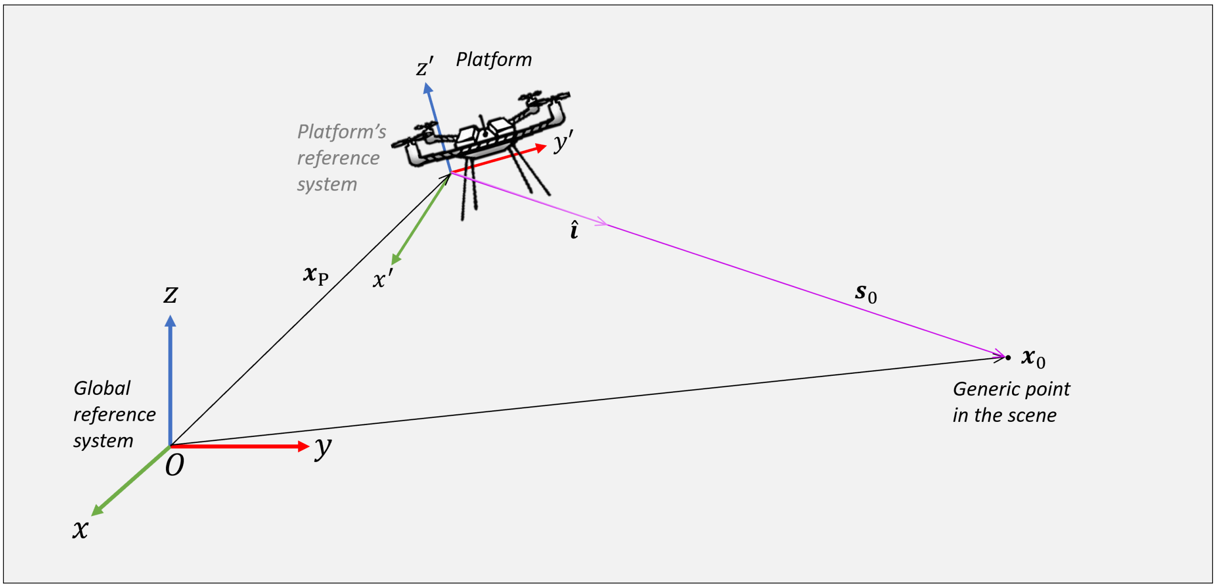

Figure 2.1 – Scenario definition.

Every object in space is identified by its position vector, denoted by $\mathbf{x}$ with a subscript, which is defined relatively to the global reference system (Fig. 2.1). The platform is placed at $\mathbf{x}_\mathrm{P}$, that also includes a time dependency to describe the trajectory of the platform. Meanwhile, the point of interest, i.e. the point-like target, is located at $\mathbf{x}_0$ and doesn't move. These points are expressed with respect to the global reference system, which is arbitrarily positioned and in general doesn't provide the perspective of either the platform or the target. For this reason, it is useful to express the position of the target, in this case $\mathbf{x}_0$, relative to the platform's centered coordinate frame. In this translated coordinate frame, the target is described by the relative position vector

$$\mathbf{s}_0 = \mathbf{x}_0 - \mathbf{x}_\mathrm{P}. \tag{2.1}$$

This vector is still expressed in global coordinates, thus it's not affected by the platform rotation, but it removes the arbitrariness of the global reference system positioning and takes into account the relative motion between platform and target. It is also helpful to name another important vector, which is the unit vector obtained from $\mathbf{s}_0$:

$$\hat{\mathbf{i}}_0 = \frac{\mathbf{s}_0}{|\mathbf{s}_0|}. \tag{2.2}$$

The $\hat{\mathbf{i}}_0$ vector is usually called ”line of sight”, because it describes the looking direction from which the platform sees the target. It also describes the propagation direction of the EM wave, therefore it's orthogonal to the wave front.

The platform, from a SAR image formation point-of-view, is only relevant when it comes to its position in space and could thus be considered as a point-like object. However, the platform mounts the antenna, which has three-dimensional properties associated with it, hence its orientation in space still matters. In order to take into account the orientation of the platform, a secondary reference system is needed, located near or inside the platform itself (Fig. 2.1). The platform's reference system is ultimately described by means of a rotation matrix R, which allows to change coordinates from the global reference system to the relative one. The rotation matrix R also changes with respect to time, accounting for both the orientation of the antenna and the rotation of the platform over the course of the acquisition. Through R, the line of sight vector can then be expressed in the coordinate frame of the platform. The usefulness of the rotated line of sight is to address both the antenna pattern and gain as functions of the looking direction. For ease of notation and clarity, these functions will in fact be addressed using just two arguments: frequency and the relative line of sight vector.

At first, the target can be thought of as an extended object, continuously spanning over the whole scene of interest. As a physical object, it can be described as being composed of different materials distributed in a certain fashion in space. Even though this sounds simple, the way this physical description maps to the electromagnetic response of the target is very complex [28]. It depends on the material composition, its distribution in space, the shape of the object, the polarization and frequency of the EM wave and the directions from which the wave comes and from where it's received. This interaction is what ultimately generates the EM response of the target for a given acquisition, and it must be simplified in order to have a meaningful way to represent the response.

The adopted model for the target, which is also a fairly flexible model, is the reflectivity function [27, Sec. 6.1]. The reflectivity function models the target as a complex function of the space coordinates. In other words, it associates at every point in space a complex number, whose amplitude represents the percentage of the incident wave that gets back-scattered. Since the EM interaction also modifies the phase of the wave, the reflectivity is a complex number multiplying the back-scattered wave [15]. In relation to the physical description of the target, the reflectivity function will have a greater amplitude around the discontinuities of the spatial material distribution, meanwhile it will be closer to zero in every other point. For instance, in air the function will evaluate to almost zero and around a metal object it would spike. In the used model, the angular dependence of the reflectivity function is neglected for simplicity, which is quite the strong hypothesis in close geometry scenarios. However, a model that takes into account this dependency would greatly complicate the treatment of the problem. In the scope of this thesis, the electromagnetic model of the target will furthermore be considered constant in frequency and for a single polarization only. Thus, the reflectivity function can be seen as the back-scatter response of the target, valid at any frequency and looking direction, to an EM wave with single polarization. This description greatly simplifies the interaction between the incident wave and the target, but it neglects some physical effects like shadowing, surface waves, the already mentioned looking angle dependence and others.

2.2 Received signal

The received signal at the end of its journey is the result of many processes and physical interactions. Starting from the signal generator, the signal propagates inside the radar front-end until it reaches the antenna. As the current carrying the transmitted signal spreads out inside the antenna, the surrounding EM field is perturbed according to Maxwell's equations, and a wave is generated as a consequence. The EM wave then propagates as predicted by the wave equations [29, eq. (15.1.7)] and, upon contact with the target, part of its power is scattered in every direction, including the one where the platform is located. The same thing happens in every point in space, resulting in a multitude of EM waves propagating towards the platform, each having its own amplitude and phase (Fig. 2.2). The resulting EM field at the antenna location is the superposition of all these EM waves. Finally, the combined EM field is transformed back into a current, that once again traverse the front-end of the radar.

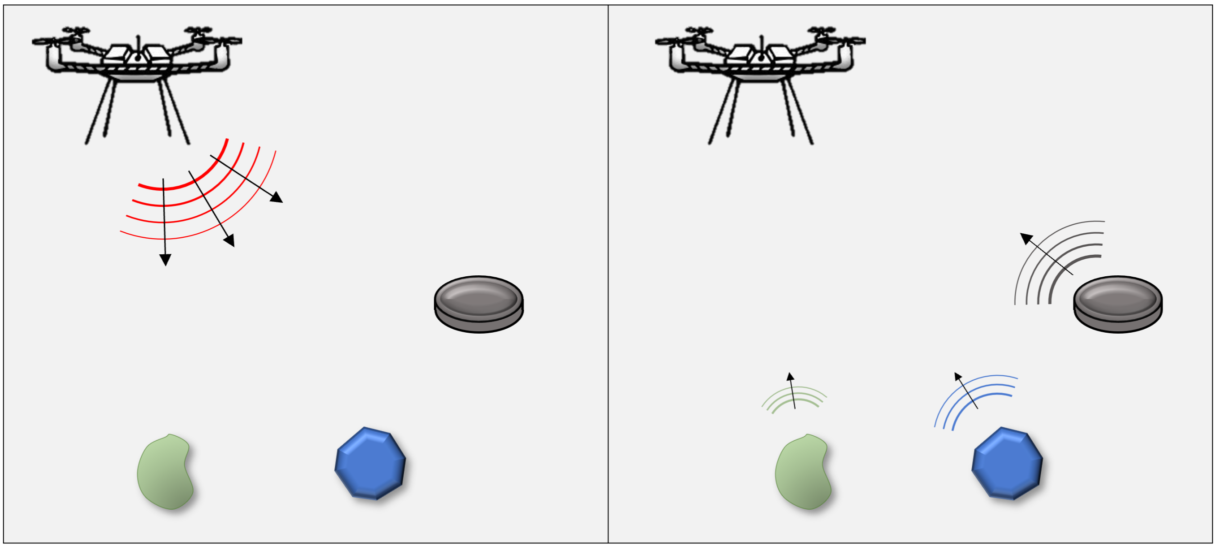

Figure 2.2 – The transmission and reception process of the EM wave.

This journey is very complicated, with the main issue being the electromagnetic interaction with the target, and a complete model that takes into account everything is rather messy to handle. Hence, there are a number of assumptions that simplify the mathematical treatment of the signal model. Through these simplifications, it is possible to focus on the structure of the signal and identify the connection between the received signal and the quantity of interest, being the radar reflectivity of the target.

First thing first, the many components present in the transceiver can be safely ignored, because they do not change the structure of the data and the image formation process. These components (amplifiers, mixer, power dividers, filters, etc.) are still a source of disturbance and should be considered in the context of internal calibration, but they are not a big source of uncertainty. Moreover, the calibration loops situated alongside these components help to keep at bay the distortions [15]. The signals considered in the model are, then, what enters the antenna's terminals, i.e. the modulated radiofrequency (RF) signal, and what comes out of them after receiving the target's electromagnetic response.

Another very important assumption to apply whenever dealing with radar signals is the ”stop and hop” approximation [30]. This hypothesis is based on the fact that the platform moves very slowly compared the EM wave. The idea, then, is to consider the platform as if it stopped during the transmission and reception of a single pulse. After a time corresponding to the pulse repetition interval (PRI), the platform would directly hop to the next transmission location, rotated accordingly. Under this hypothesis, there are two direct consequences that simplify the EM wave description. Firstly, the Doppler effect [29, Sec. 2.12] can be ignored, as everything is stationary, hence the signal delay is constant within every pulse. The delay still changes over time, but only from one pulse to the other. Then, it is possible to split time into two orthogonal dimensions: the continuous *fast-time*, which is used to address time inside the PRI, and the inherently discrete *slow-time*, which is used to address the different pulses. Slow-time can directly be mapped to the set of integers, thus the notation henceforth used to identify the pulse number and the relative slow-time instant will be an n index. Every quantity that changes slowly and discretely over time will have an n index as an appendix to represent their dependence on slow-time. Meanwhile, the time variable t will always represent fast-time.

The other consequence of the ”stop and hop” hypothesis is a simplification of the EM wave nature. By definition, the EM wave is a multi-dimensional (space-time dependent) vector field, which is characterized by numerous properties, meanwhile its starting point is a mono-dimensional (time dependent) scalar signal. Nonetheless, this complexity can be ignored in the stationary scenario described above. Indeed, the EM wave received from a particular direction will be polarized the same way as the incident wave propagating in the same direction, therefore it is not necessary to consider its vector nature. For all purposes, it is as if the EM wave was a scalar field. In conjunction to this, the electromagnetic interaction with the target is further simplified. The above description for the signal path implies multiple scattering of the EM wave inside the target, giving rise to a non-linear relationship between the incident wave and the total scattered wave. Applying the Born approximation [27, Sec. 6.4] to the scattered wave is key to obtain a useful signal model. Thanks to this assumption, valid in case of low power transmissions, the EM interaction with the target can be simplified to a linear relationship by neglecting the higher-order scattering contributions.

Lastly, the received signal model is presented, as derived in [27, Ch. 6] using all the due approximations:

$$s_{\mathrm{R}}^{(n)}(t) = -\int \frac{\ddot{s}(t - 2|\mathbf{x} - \mathbf{x}_{\mathrm{P}}^{(n)}|/c)}{(4\pi|\mathbf{x} - \mathbf{x}_{\mathrm{P}}^{(n)}|)^2} q(\mathbf{x}) d^3\mathbf{x}, \tag{2.3}$$

where $s(t)$ and $\ddot{s}(t)$ are the transmitted signal and its second derivative, $\mathbf{x}_{\mathrm{P}}^{(n)}$ is the position of the platform at the $n-$th pulse, $q(\mathbf{x})$ is the reflectivity function of the target and c is the speed of light in air or vacuum.

As expressed above, the dependence of the received signal on delays, and hence on ranges, is bound to the particular transmitted waveform. Unless the exact signal is specified, this information cannot be extracted. This is why it is very helpful to make use of the Fourier transform and its properties. In fact, a useful property of the Fourier transform is its ability to convert a delay in time domain into a phase term in frequency domain. As a consequence, all the copies of the signal $s(t)$, each delayed by a different amount, will fall into the same frequency band, alongside their corresponding phase term.

The end result is:

$$S_{\mathrm{R}}^{(n)}(\omega) = \int \frac{e^{-j2k|\mathbf{x} - \mathbf{x}_{\mathrm{P}}^{(n)}|}}{(4\pi|\mathbf{x} - \mathbf{x}_{\mathrm{P}}^{(n)}|)^2} \omega^2 S(\omega) q(\mathbf{x}) d^3\mathbf{x}, \tag{2.4}$$

where $k = \omega/c$ is the wavenumber, which corresponds to a spatial frequency.

2.3 Received signal affected by the antenna gain

The antenna generates a spherical EM wave that propagates into space like an inflating balloon. Although it propagates in every direction at the same time, not every direction is regarded the same. Far away from the antenna, the variations in the wave amplitude can be modeled solely as a function of frequency and propagation direction, removing the dependence on the sphere's radius r like so:

$$E(\omega, r, \phi, \theta)\, e^{jkr} r = f(\omega, \phi, \theta), \tag{2.5}$$

where E is the relevant component of the electric field [29, eq. (15.10.2)] for the chosen polarization. The function f thus obtained is proportional to the same polarization component of the radiation vector [29, eq. (15.7.5)], and represents the field radiation pattern [31, Sec 2.2]. In its definition, the radiation vector also contains the transmitted signal, which is carried by the current I_0 entering the antenna's terminals. Dividing the function f by the current, a new function can be obtained,

$$h(\omega, \phi, \theta) = \frac{f(\omega, \phi, \theta)}{I_0(\omega)}, \tag{2.6}$$

that encompasses only the antenna's influence on the transmitted EM wave. Being f proportional to a component of the radiation vector, the function h is proportional to the same component of the effective length [29, eq. (16.5.1)]. While deriving the signal model in (2.4), this function has been assumed to be constant. However, the non-uniform weighting introduced by the antenna must also be investigated for the sake of internal calibration, especially for UAV-SAR systems, hence it must be included in the model.

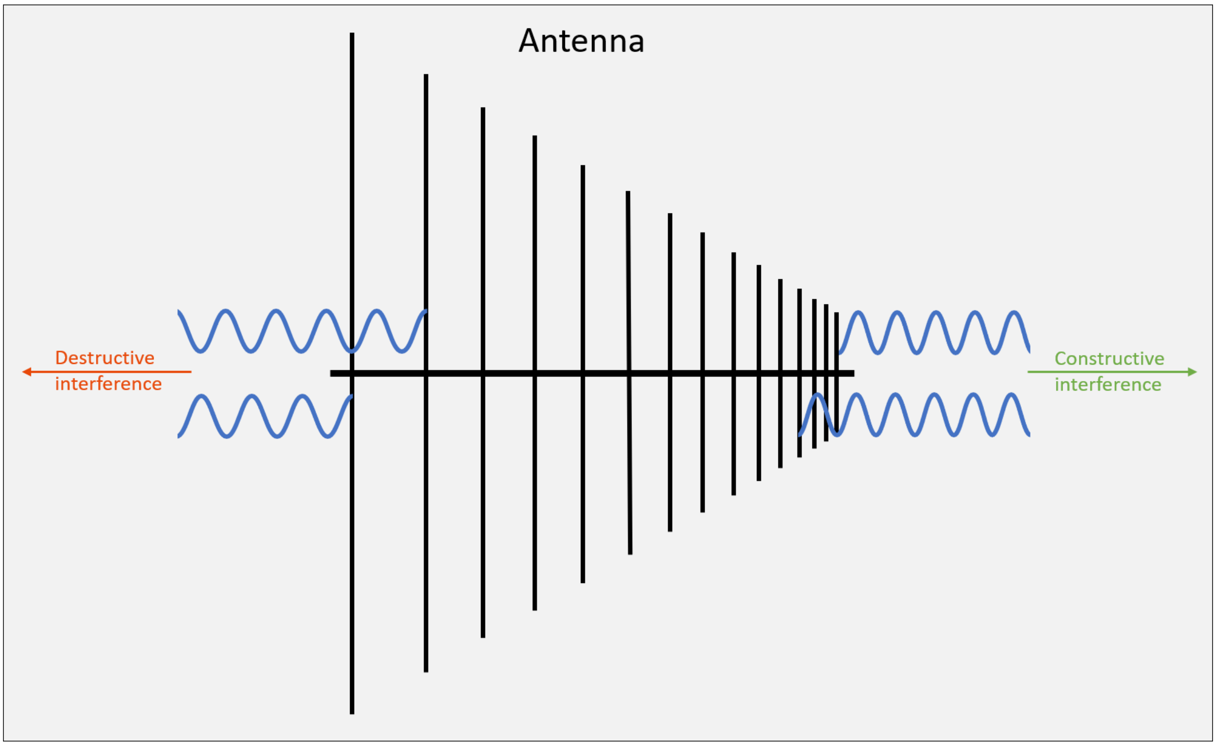

Figure 2.3 – The antenna radiation pattern property explained as the effect of interference.

The radiation pattern is a property that originates from the transmission of the EM wave, through the mechanism of interference (the integral in [29, eq. (15.7.5)] is a summation of waves originating from every point of the antenna, as illustrated in Fig. 2.3). Nonetheless, due to the reciprocity principle, it also describes how the antenna weighs the received waves coming from each direction [32]. During a single acquisition, the platform is stationary, so the EM wave coming from one direction is the aftermath of the wave propagating in the same looking direction, $R^{(n)}\hat{\mathbf{i}}^{(n)}$. Consequently, the amplitude is weighted twice by the same pattern value: $h(\omega, R^{(n)}\hat{\mathbf{i}}^{(n)})$ when transmitting and $h(\omega, R^{(n)}\hat{\mathbf{i}}^{(n)})$ when receiving. The product of the two, $h^2(\omega, R^{(n)}\hat{\mathbf{i}}^{(n)})$, is the complex field pattern that the target's response experiences. In order to simplify the investigation, the complex nature of the radiation pattern is neglected, assuming the phase to be zero over every frequency and direction. Under this hypothesis, the squared antenna pattern is proportional to the antenna power gain at the same frequency and looking direction. For all intents and purposes, it will be considered to be equal to the gain of the antenna, ignoring the proportionality factors. These factors do not influence the effect the antenna has on the received signal, therefore the results and conclusions reached at the end are still valid.

In light of this, the complete signal model in frequency domain is:

$$S_{\mathrm{R}}^{(n)}(\omega) = \int \frac{e^{-j2k|\mathbf{x}-\mathbf{x}_{\mathrm{P}}^{(n)}|}}{(4\pi|\mathbf{x}-\mathbf{x}_{\mathrm{P}}^{(n)}|)^2} \omega^2 S(\omega) G(\omega, R^{(n)}\hat{\mathbf{i}}^{(n)}) q(\mathbf{x}) d^3\mathbf{x}, \tag{2.7}$$

where G is the antenna gain and the line of sight vector is here a function of the integration variable $\mathbf{x}$:

$$\hat{\mathbf{i}}^{(n)} = \frac{\mathbf{x}-\mathbf{x}_{\mathrm{P}}^{(n)}}{|\mathbf{x}-\mathbf{x}_{\mathrm{P}}^{(n)}|}.$$

2.4 Far-field approximation

The far-field approximation is a very common simplification in the field of electromagnetism. In order to apply it, it is convenient to subdivide the extended target into contiguous spatial domains from which the signal is received (Fig. 2.4). Thanks again to the Born approximation, the total received signal is given by the summation of the individual contributions originating from every partition of the target. In the following treatment, only a single partition, from here on simply ”the target”, is considered as a contributor to the received signal, so that the data structure can be highlighted. A more comprehensive analysis taking into account multiple targets will be carried on in Ch. 5. This description of the extended target allows to freely decide the size of each individual target, with the consequence that the number of targets increases the smaller each partition gets. The advantage of deciding the target's size is that it can always be small enough to respect the conditions necessary for the approximation to be true.

The role of the far-field hypothesis is to linearize the distance between the platform and each point inside the target, by assuming the target is small compared to the distance that separates it

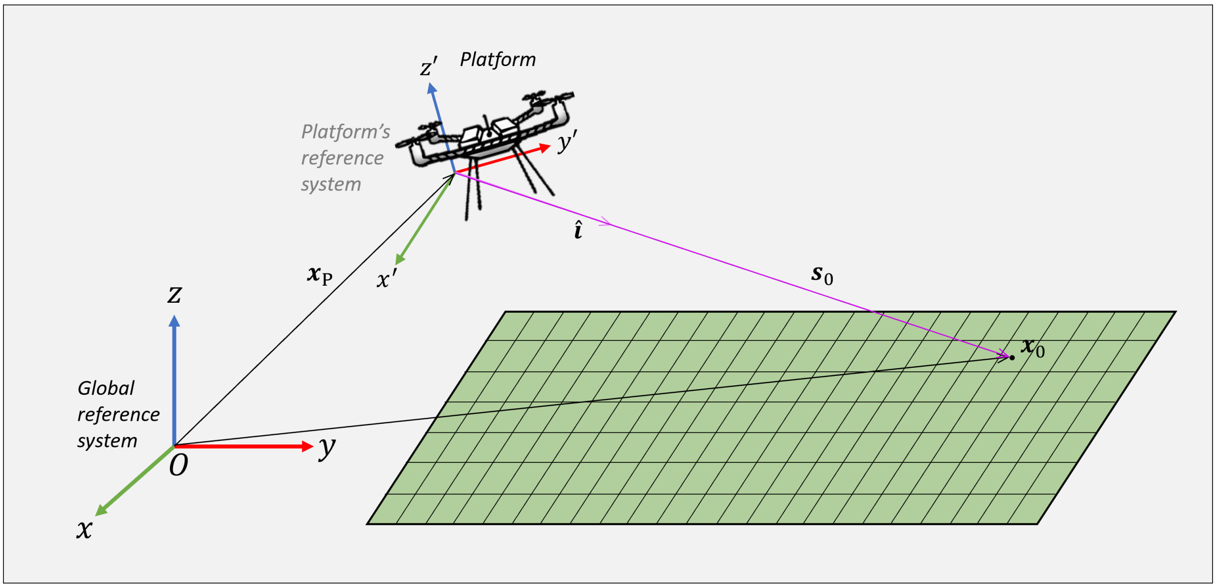

Figure 2.4 – A flexible target description: the reflectivity function can be subdivided into smaller segments.

from the platform. The distance between the platform and a point $\mathbf{x}$ inside the target is $|\mathbf{x} - \mathbf{x}_{\text{P}}|$, in which the slow-time index is omitted for better readability. This distance is a non-linear function of the position vector $\mathbf{x}$, therefore it complicates the mathematical treatment of the signal model. Assuming the target is located in $\mathbf{x}_0$, the function can be rewritten as

$$d_{\mathbf{x}_{\text{P}}}(\mathbf{x}) = |\mathbf{x} - \mathbf{x}_{\text{P}}| = |(\mathbf{x}_0 - \mathbf{x}_{\text{P}}) - (\mathbf{x}_0 - \mathbf{x})| = |\mathbf{s}_0 - (\mathbf{x}_0 - \mathbf{x})| = d_{\mathbf{s}_0}(\mathbf{x}_0 - \mathbf{x}), \tag{2.8}$$

highlighting the two distances upon which the approximation acts on. If the target is small compared to the distance $|\mathbf{s}_0|$, then for every point $\mathbf{x}$ inside the target the following relations are valid:

$$\begin{aligned} d_{\mathbf{s}_0}(\mathbf{x}_0 - \mathbf{x}) &\approx |\mathbf{s}_0|, \\ d_{\mathbf{s}_0}(\mathbf{x}_0 - \mathbf{x}) &\approx |\mathbf{s}_0| - \hat{\mathbf{i}}_0 \cdot (\mathbf{x}_0 - \mathbf{x}), \end{aligned} \tag{2.9}$$

where $\hat{\mathbf{i}}_0$ is the unit vector obtained from $\mathbf{s}_0$.

The approximations in (2.9) are the zeroth- and first-order expansions of $d_{\mathbf{x}_{\text{P}}}(\mathbf{x})$ around the point $\mathbf{x} = \mathbf{x}_0$. Looking at the second line of (2.7), the distance is found in the denominator of the integrand and as the argument of the complex sinusoid. The former relation depends on the absolute value of the distance, which changes slowly as a function of $\mathbf{x}$, meanwhile the latter depends on the distance modulo $\lambda/2$, therefore it is sensible to changes even at a great distance. The amplitude can then be approximated using the zeroth-order expansion, while the phase must be approximated with at least the first-order expansion. The necessary conditions needed by the far-field hypothesis are [27, Sec. 7.1]:

$$\begin{aligned} |\mathbf{x}_0 - \mathbf{x}| &<< |\mathbf{s}_0|, \\ k|\mathbf{x}_0 - \mathbf{x}|^2 &<< |\mathbf{s}_0|. \end{aligned} \tag{2.10}$$

2.5 Interpretation of the received signal

The received signal, expressed in frequency domain and simplified by means of the far-field approximation, results in:

$$\begin{aligned} S_{\mathrm{R}}(\omega) &\approx \int_{V_0} \frac{e^{-j2k|\mathbf{s}_0|} e^{j2k\hat{\mathbf{i}}_0\cdot(\mathbf{x}_0-\mathbf{x})}}{(4\pi|\mathbf{s}_0|)^2} \omega^2 S(\omega) G(\omega, R\hat{\mathbf{i}}) q(\mathbf{x}) d^3\mathbf{x} = \\ &= \frac{e^{-j2k|\mathbf{s}_0|}}{(4\pi|\mathbf{s}_0|)^2} \omega^2 S(\omega) \int_{V_0} G(\omega, R\hat{\mathbf{i}}) q(\mathbf{x}) e^{j2k\hat{\mathbf{i}}_0\cdot(\mathbf{x}_0-\mathbf{x})} d^3\mathbf{x}, \end{aligned} \tag{2.11}$$

where V_0 is a small volume centered in $\mathbf{x}_0$ containing the target. Once again, all the slow-time indexes are omitted for better readability. Before proceeding with the analysis of the received signal structure, it is best to center the reflectivity function around the target in $\mathbf{x}_0$. Let $q_0(\mathbf{x})$ be the reflectivity function of the target in volume V_0, such that

$$q_0(\mathbf{x}) = \begin{cases} q(\mathbf{x} + \mathbf{x}_0) & \text{if } (\mathbf{x} + \mathbf{x}_0) \in V_0 \\ 0 & \text{otherwise} \end{cases},$$

then the signal model can be written as:

$$S_{\mathrm{R}}(\omega) = \frac{e^{-j2k|\mathbf{s}_0|}}{(4\pi|\mathbf{s}_0|)^2} \omega^2 S(\omega) \int G(\omega, R\hat{\mathbf{i}}) q_0(\mathbf{x} - \mathbf{x}_0) e^{-j2k\hat{\mathbf{i}}_0\cdot(\mathbf{x}-\mathbf{x}_0)} d^3\mathbf{x}. \tag{2.12}$$

The gain within the integral varies across the portion of the field of view occupied by the target in V_0, but it can be approximated as constant for a small target. Since the target can be chosen to be as small as desired, like discussed in the previous section, the approximation is valid to any extent. Thus, the gain value multiplying the reflectivity function can be brought out of the integral and considered equal to the value in direction $R\hat{\mathbf{i}}_0$:

$$\begin{aligned} S_{\mathrm{R}}(\omega) &= \frac{e^{-j2k|\mathbf{s}_0|}}{(4\pi|\mathbf{s}_0|)^2} \omega^2 S(\omega) G(\omega, R\hat{\mathbf{i}}_0) \int q_0(\mathbf{x} - \mathbf{x}_0) e^{-j2k\hat{\mathbf{i}}_0\cdot(\mathbf{x}-\mathbf{x}_0)} d^3\mathbf{x} = \\ &= \frac{e^{-j2k|\mathbf{s}_0|}}{(4\pi|\mathbf{s}_0|)^2} \omega^2 S(\omega) G(\omega, R\hat{\mathbf{i}}_0) \int q_0(\mathbf{y}) e^{-j2k\hat{\mathbf{i}}_0\cdot\mathbf{y}} d^3\mathbf{y}, \end{aligned} \tag{2.13}$$

where in the second line the change of variable $\mathbf{y} = \mathbf{x} - \mathbf{x}_0$ has been made.

The final result shows a rather simple relationship between the received signal and the quantity of interest, i.e. the reflectivity function. Ignoring the factors out of the integral, what's left is the Fourier transform of the reflectivity function in three dimensions, calculated at the spatial frequency

$$\mathbf{k} = 2k\hat{\mathbf{i}}_0 = \frac{2\omega}{c}\hat{\mathbf{i}}_0,$$

so that

$$S_{\mathrm{R}}(\omega) = \frac{e^{-j2k|\mathbf{s}_0|}}{(4\pi|\mathbf{s}_0|)^2}\omega^2 S(\omega)G(\omega, R\hat{\mathbf{i}}_0)Q_0(2k\hat{\mathbf{i}}_0), \tag{2.14}$$

where

$$Q_0(\mathbf{k}) = \mathcal{F}\{q_0\}(\mathbf{k}) = \int q_0(\mathbf{y})e^{-j\mathbf{k}\cdot\mathbf{y}}d^3\mathbf{y}. \tag{2.15}$$

The three-dimensional Fourier transform of the reflectivity function is defined over the whole spatial frequency domain, but only a one-dimensional slice of $Q_0(\mathbf{k})$ is available with each acquisition. The direction from which the target is viewed determines the direction of the frequency points acquired, meanwhile the signal bandwidth limits the radial component of the spatial frequency, because k is proportional to ω. In this regard, the transmitted signal $S(\omega)$ acts like a windowing function of the radial component.

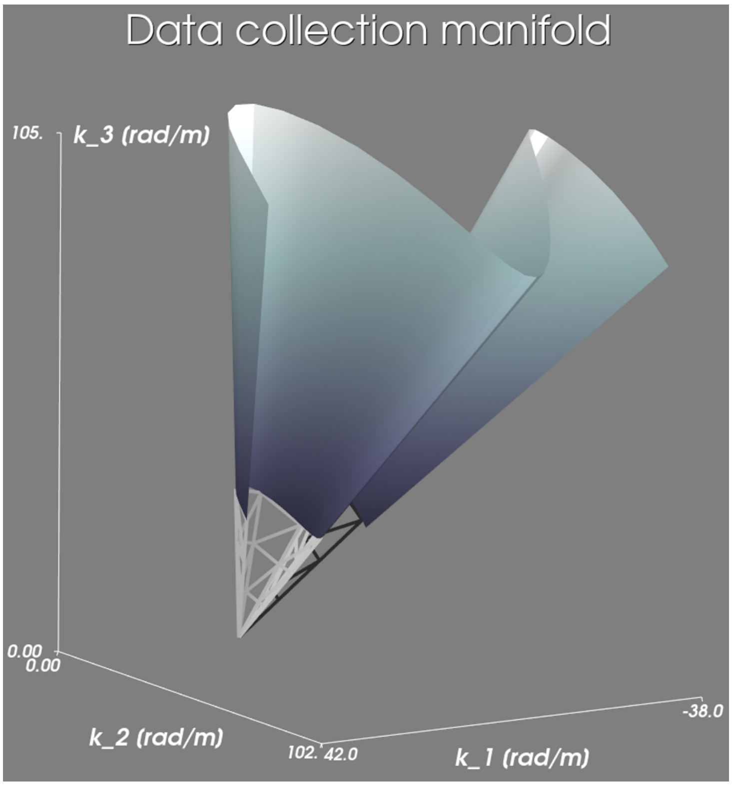

Figure 2.5 – Example of a data collection manifold for a single point-like target. The 2D surface represent the domain of the available data in the 3D spatial frequency space.

The collection of all received signals from each pulse gives rise to the data collection manifold, which can be seen in Fig. 2.5. The region in the spatial frequency domain described by the data collection manifold is all the information available for the observed target. Since the observed slice of $Q_0(\mathbf{k})$ depends on $\hat{\mathbf{i}}_0$, which ultimately depends on the position of the platform, the shape of the data collection manifold depends on the particular acquisition geometry, which then acts like a windowing function of the viewing angles. In general, the more observations about the target, the more data can fill in the void. Still, the limit given by the bandwidth of the transmitted signal can only be overcome by increasing the actual bandwidth. Taking into account the whole subdivided target though, each partition has a different portion of the Fourier transform of its reflectivity function available, because the line of sight vector $\hat{\mathbf{i}}_0$ also depends on the position of the partition.

2.6 SAR processing and the point spread function

Considering the relatively straightforward structure of the data in (2.14), a SAR processing algorithm needs only to implement a three-dimensional inverse Fourier transform of the data. The inverse Fourier transform can be implemented in many ways, giving birth to very different algorithms. In general though, and in particular for UAV-SAR scenarios, no assumptions can be made about the acquisition geometry, and thus about the shape of the data collection manifold. As a result, the only way to compute the SAR image is by applying the actual inverse Fourier transform to the received data. However, there is still a choice on how to implement the full-fledged inverse Fourier transform. Transforming (2.14) back into time domain through the use of the projection-slice theorem [33], enables the connection between SAR processing and the, apparently, far away world of computer aided tomography (better known as CAT), as indicated in [34]. Therefore, it is possible and very convenient to apply the back-projection algorithm [35] to the time-domain received signal. Regardless of the chosen implementation, the end result should remain consistent.

In order to apply any SAR processing to the data, the terms that multiply the Fourier transform $Q_0(\mathbf{k})$ in (2.14) must be compensated. This step is ultimately the task of the internal calibration procedure. However, a perfect calibration method does not exist and the resulting SAR image will be a distorted version of the reflectivity function of the target. Analyzing the distortions would help to understand what is shown in the images and how it relates to the real observed scene. Doing so requires to have a quantitative description of the relationship between the SAR image and the quantity being imaged.

The point spread function (PSF) aims to give such a description of the entire SAR imaging system. It is defined as the response of the system to a point-like target [15, Sec. III], therefore it includes all possible effects introduced on the received signal, but removes the contribution of the target itself. Setting the target's reflectivity function to be a Dirac's delta, its Fourier transform $Q_0(\mathbf{k})$ is constant over the whole frequency domain. Then, the system's response function can be defined in spatial frequency domain directly from (2.14), collecting all the received signals:

$$H(\mathbf{k}) := S_{\mathrm{R}}(\mathbf{k}) = W(\hat{\mathbf{k}}) \frac{e^{-j|\mathbf{k}||\mathbf{s}_0|}}{(4\pi|\mathbf{s}_0|)^2} |\mathbf{k}|^2 S(|\mathbf{k}|) G(\mathbf{k}), \tag{2.16}$$

where $W(\hat{\mathbf{k}})$ is a windowing function of the looking directions. The combination of W and the transmitted signal S produces an overall windowing function valid over the data collection manifold. This function takes into account the effects of the limited data availability both in looking direction and radial component. Its presence alone determines a distortion that spreads the energy of the point-like target all over the neighboring pixels in the image, lowering the resolution. In addition to this, the other terms modulate the windowing function, producing even more distortions.

Through this description of the system, it would then be possible to analyze the type of distortions present in the image and how they interact with each other. However, the PSF includes in its definition terms that strictly depend on the particular acquisition geometry and on the position of the target, hence the transfer function is space-variant and it can only be numerically computed for every target in the scene. Consequently, it is not possible to predict analytically the exact distortions and properties of the system at hand. Ideally, the PSF would be a constant function in frequency domain, thus yielding the desired image of the reflectivity function without distortions. Due to the lack of information about $Q_0(\mathbf{k})$, it is impossible to achieve such an ideal result, with the extent of the data collection manifold that controls the resolution and quality of the reconstructed reflectivity function. Then, the PSF should at least be constant over the domain of the available data. Such is the goal of the internal calibration.

Chapter 3

THE SIMULATOR: DESCRIPTION AND FIRST RESULTS

In order to investigate the applicability and performance of existing calibration procedures in the realm of UAV-SAR systems, a simulation framework is essential. The usefulness of the SAR simulator extends even past the experimental results, thanks to its ability to create a sandbox environment. Inside the simulation, it is possible to control everything very precisely and exclude undesired effects. It is possible to achieve every acquisition geometry, do as many simulations as desired, easily tweak system parameters and so on. For instance, in the scope of this thesis, noise is neglected in any simulation. However, aside from noise, the simulator is designed to be as close as possible to the radar system and the physical world, within reason. The whole simulation environment is designed upon the definitions given in Ch. 2 and the simulator is written in Python, making use of the NumPy library [36].

3.1 Structure of the simulator

The final product aims to be a flexible SAR simulation software capable of adapting to every system and scenario. In order to achieve this level of flexibility, a set of guidelines has been established to guide development. An important key feature of the program is the module organization. A Python module is a standalone file that contains any kind of code, which can then be executed from another module. Keeping the various aspects of the simulator, like the geometry, platform, target and so on, separate allows to better organize the simulator structure (Fig. 3.1), shortening the code length of the main module and maintaining readability. Albeit helpful in its own way, the module organization is supported with a completely parameterized code that ensures flexibility. Every module uses what has been defined in other modules, so as long as data types, data organization, variable and function names all remain the same, the code execution is guaranteed regardless of the definitions provided by the user. It is then possible to change any module without resulting in a disruptive behavior of the simulation, because the other modules are left unaffected. Thanks to these two intertwined guidelines, a solid base for flexibility is laid, upon which everything can be built. Furthermore, the user could even provide actual data in every module, instead of simulating it. Again, following the guidelines, the real data would then play along with the simulated data in the program execution and everything would work accordingly.

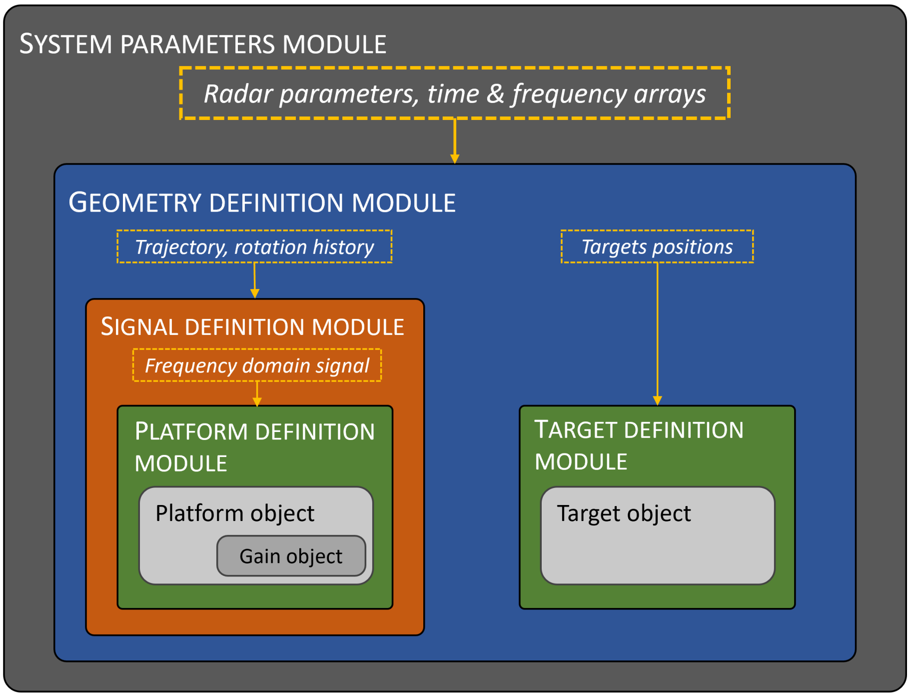

Figure 3.1 – The simulator structure and module organization.

Another benefit of using different modules is the ability to execute them individually. Every module has some kind of visualization, shown only if the specific module is run as the main program, which helps to investigate any problem with the scenario configuration or the module itself. Moreover, the visualizations show in detail every aspect of the simulation, like the geometry, the transmitted or received signal, the antenna gain and more. In this regard, a special data visualization module was also created. The main purpose of this module is to plot saved data without having to wait for the simulation to generate it again, but it also contains a set of plotting functions. These functions are specific to the SAR simulator, but at the same time they are general enough to be used by all modules to plot various types of data.

3.1.1 Scenario and system definition

There are three modules that define the scenario entirely. All the other modules are parameterized after these, so the user don't have to search around the simulator to change the configuration. In a future implementation, there could be a single module, or even better some sort of graphical interface, in which every aspect of the simulation can be controlled and configured.

Starting with the parameter definitions, they are all contained into one module, named `system parameter`. Most of the parameters are related to the radar system, as part of its design and hardware composition, but there are also parameters regarding the signal definition and the spatial image boundaries and digital resolution. In addition to the parameters, the time, frequency and spatial arrays are defined in this module, as they are necessary throughout the whole simulation. Some parameters are also defined as needed in the `geometry definition` module. Fundamentally, the geometry is composed of the targets positions and the trajectory of the platform. Still, the simulator also has to account for the rotation of the platform, which is provided in terms of the roll, pitch and yaw angles. Lastly, the signal is defined in the `signal definition` module. The signal used by the simulator is always expressed in frequency domain, for reasons that will be explained later on, but the generation is not limited to the frequency domain. There are two functions that create the signal in either time or frequency domain, implementing the analytical or algorithmic definitions given by the user. The module then proceeds to compute the array relative to the frequency domain signal. In case of need, multiple signal arrays could be instantiated, using different definitions. In Fig. 3.2 is shown an example of a scenario. The plots are generated by the modules themselves.

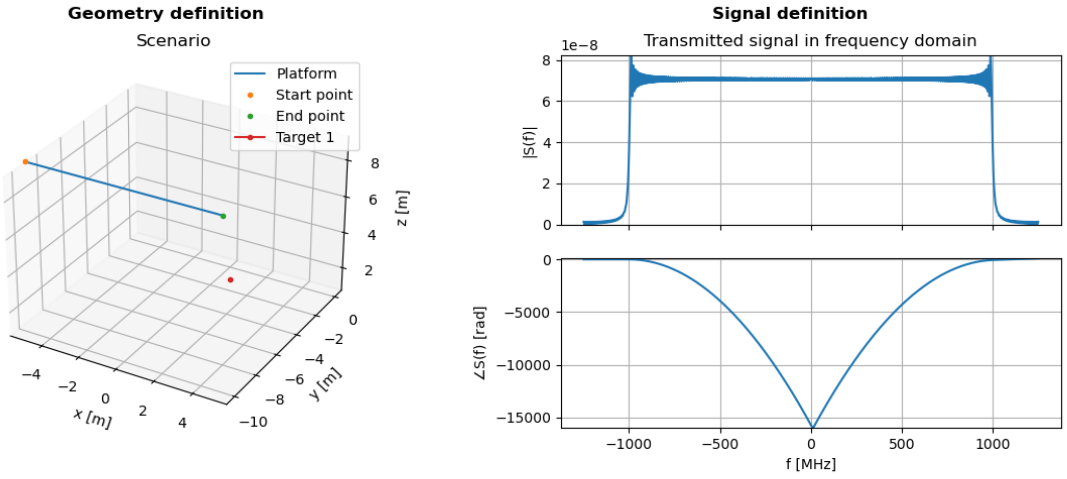

(a) **(b)**

Figure 3.2 – Example of a scenario configuration.

3.1.2 Platform definition

The `platform definition` module actually contains the definition of two classes: the platform and the antenna gain. It is useful to have a class to handle the gain, because the same antenna could be mounted on different platforms. Thus, the proposed simulator framework is capable of simulating generic multi-static configurations.

A gain object can be defined through the gain class initialization function, which allows to specify the gain values and the relative points over which they are defined. Since the gain is a function of frequency and looking direction, the definition points are given by three arrays: the frequency, phi and theta arrays. The function also accepts a file path to load the gain from the disk, usually obtained from a full-wave simulator or a measurement instrument. In this case, the `loadAntennaGain` static method provides the instructions to load the content of the file into the newly created object. Regardless of how the initialization is performed, the gain, frequency and angles arrays become the attributes of the object. Whenever it is needed to access the gain values for a specified set of frequency, phi and theta points, the method `getGain` takes as input the three arrays and returns the gain values corresponding to every combination of the input points. The usefulness of the method is not limited to a mere interface to access the gain, it also interpolates in both frequency and looking direction the gain values. In a similar fashion, the method `getGainHistory` also enables to access the gain, but instead of computing the gain for every combination of phi and theta points, it stacks the two arrays together to represent a list of looking directions. Then, the returned gain values are referred to every combination of looking directions and frequencies. The `getGainHistory` method is used to calculate the gain values seen by a target during the whole acquisition.

The platform object includes the antenna gain object as an attribute, which can be passed as an argument during initialization or directly created by the initialization function itself. The other attributes are the trajectory and rotation history, the signal and its frequency array and, lastly, the antenna pointing direction. The signal is included in the platform as an attribute to enable different platforms to have different signals. It is also used to define the matched filter of the radar system, therefore it is important even for receiving platforms. Meanwhile, the pointing direction parameter is used to specify how the platform should mount the antenna and it is relative to the platform's reference system. The pointing direction can be modified through the method `pointAntenna`, specifying a looking direction and, optionally, even a roll angle. The other methods in the platform class overwrite the ones defined in the antenna gain class. Before calling the corresponding methods of the gain class, they rotate the input directions so that the final result is to have oriented the antenna in the desired orientation. Since the gain provided by the user could be oriented randomly in its own reference frame, the orientation happens in two stages. The methods first point the antenna in a predefined direction, thus offsetting the orientation of the gain object, then they point it where specified by the corresponding attribute in the platform object. The pointing direction of the gain object is defined as the gain maximum direction. In the case of the `getGainHistory` method, the directions are rotated to also include the rotation of the platform.

In Fig. 3.3 is presented the gain used for the simulations in this thesis, which has been obtained from a full-wave simulation of an in-house antenna developed for a UAV-SAR system. The gain in Fig. 3.3a is obtained from the gain object, meanwhile in Fig. 3.3b it comes+ from the platform object. The gain object returns the gain values in its own reference frame, in which the antenna is pointing towards $+z$, meanwhile the platform object mounts the antenna with a certain orientation.

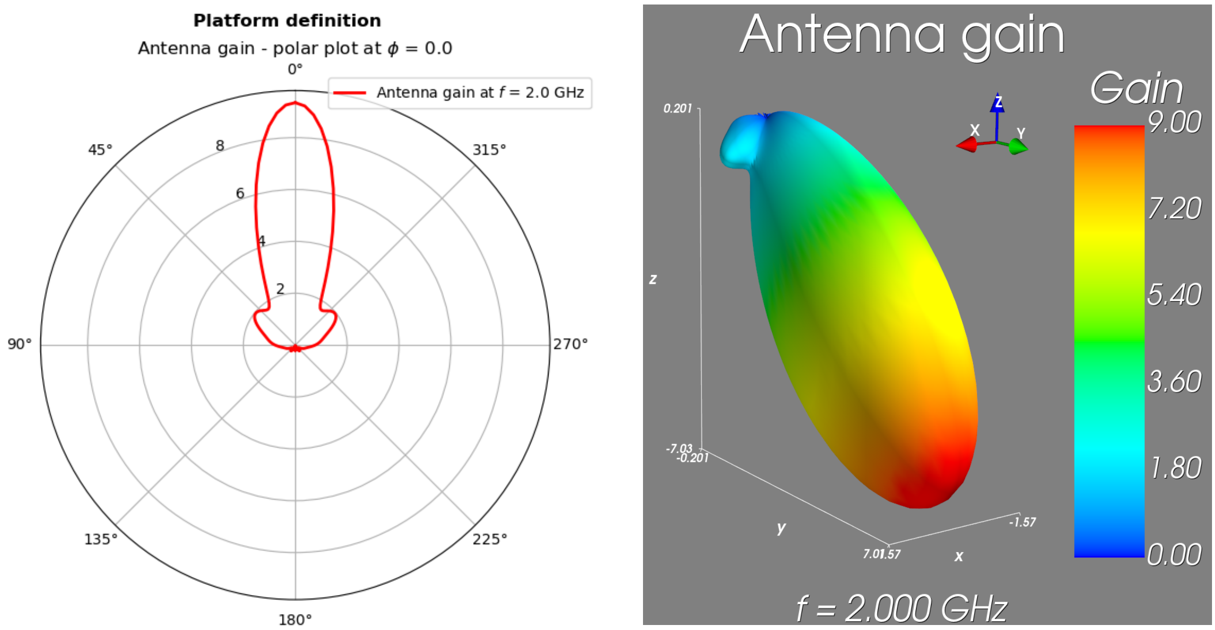

(a) **(b)**

Figure 3.3 – Plots of the antenna gain used: on the left (a) the polar plot of a section at $\phi = 0$, on the right (b) the full 3D plot of the rotated gain. The orientation of the antenna in (b) is: $(\phi_0, \theta_0) = (\pi/2, 3\pi/4)$.

3.1.3 Target definition

The target is also defined as a class, inside the `target definition` module. Simulating a target that is anything but a point-like object requires the use of specialized EM software, therefore the simulator is only capable of handling point-like targets. Nonetheless, the ground is set for future development. A feasible option would be to include a method to load the simulated response of a complex target from various directions and frequencies. Another class method would then generate the target response for a specified looking direction, eventually interpolating the available data.

The target class contains attributes that identify it in space, i.e. the position, and the peak value of its reflectivity function, which is otherwise normalized. The reflectivity function is implemented as a class method and it just returns the Kronecker's delta [37] in three dimensions (Fig. 3.4 shows the 2D cut of the reflectivity function at $z = 0$). The object initialization function can, however, accept an external function to be used as the target reflectivity function. Even though it is not as precise as a full-wave simulator, in a future implementation the simulator could integrate the provided reflectivity function to generate a more sophisticated target response.

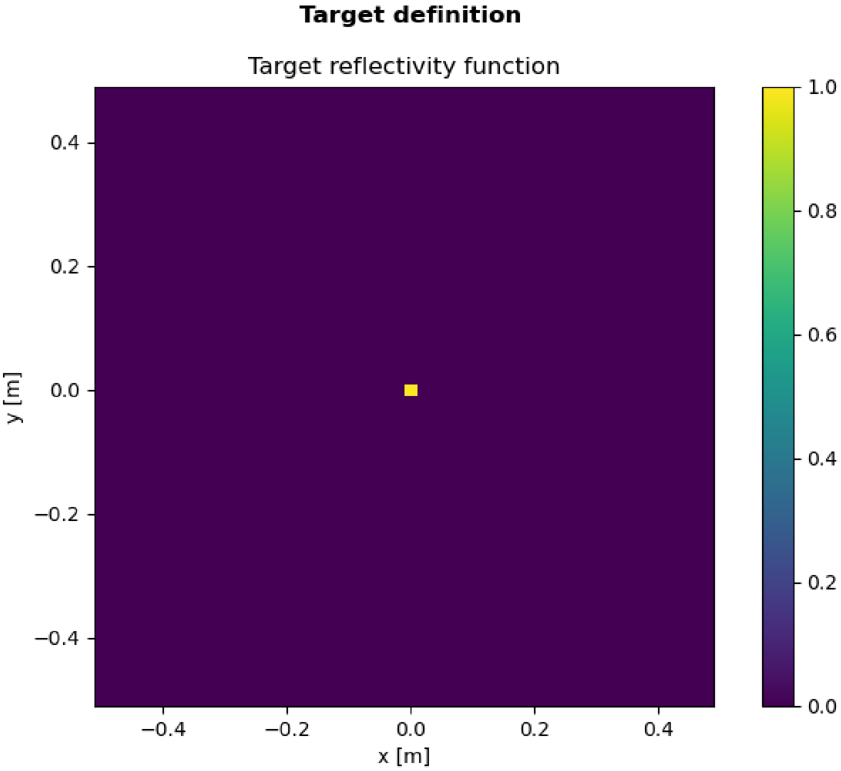

Figure 3.4 – The simulated reflectivity function of a point-like target.

3.2 Simulation flow

Among the various modules, there is the main module of the program, in which the actual simulation happens. The definition modules described above serve the purpose to define and instantiate all the required elements to simulate the received signal. In fact, everything converge into the creation of the received signal, which is the end result of the simulator. Fig. 3.5 illustrates the simulation stream.

At this stage, the simulated signal would, ideally, be the same as the one obtained by an actual radar system acquiring data in the same scenario. Therefore, the simulation can be considered finished and the program proceeds to process the data.

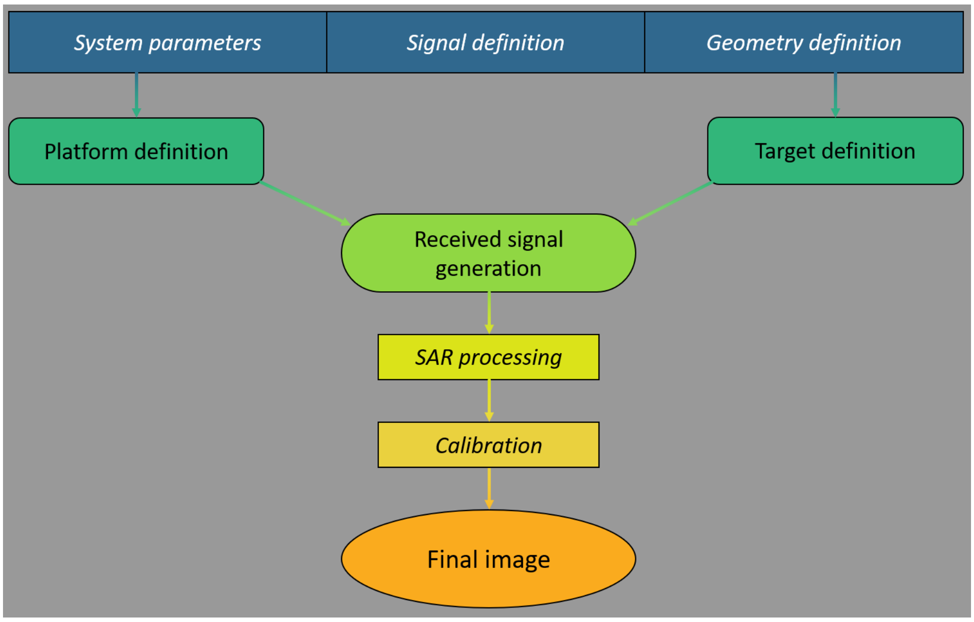

Figure 3.5 – Simulation flow: from the scenario definition, the creation of the actors involved, to the generation of the signal and finally the processing that lead to the SAR image.

3.2.1 Received signal generation

The received signal generation is a direct implementation of (2.7), in which the reflectivity function is assumed to be a sum of Dirac's deltas. The algorithm works by iterating over every target defined in the scene and generates the individual responses from each target, as if only one target was present. At the end of the loop, the total received signal is computed as the sum of the many signals received from the targets, assuming the Born approximation to be true. Thanks to this approach, there are no sources of disturbance or noise present in the signal and only the effects of the system itself can be evaluated.

Inside the loop, the algorithm calculates the physical effects that apply to the transmitted signal. Firstly, the relative position of the selected target, with respect to the platform, is processed for every slow-time instant at once. The relative vectors are then converted in spherical coordinates, which yields both the distance between platform and target and the viewing angles. Using the distance, it is possible to directly compute the delay and the free space attenuation of the EM wave, as it travels to the target and back. Meanwhile, the viewing angles are used to access the gain history for the particular target through the dedicated method, which also takes into account the rotation of the platform. Afterwards, the target's reflectivity function is evaluated at the target's location and everything is applied to the transmitted signal. The generation happens in fast-time frequency domain, thus the double derivation is also computed as a separate contribution, i.e. the term ω^2, that multiplies the signal. At the end of the generation, the signal is transformed back into time domain and what is obtained is a two-dimensional array, that represents the whole received signal subdivided into pulses. The first dimension is slow-time and the second is fast-time. Fig. 3.6 shows the received signal in time domain as a two-dimensional image, in which the signal has been interpolated to aid visualization.

There are different reasons why the generation of the received signal is performed in frequency domain, which are summarized by the two following advantages: better precision and less computational burden. To explain the first, it must be noted that the generated signal is inherently discrete inside any digital system. Hence, delaying the transmitted signal in time domain is limited by the sampling rate; even if the delay is calculated exactly, the effective delay will be approximated. Instead, in frequency domain the delay transforms into a phase term and the approximation is virtually nonexistent. Consequently, the sampling rate can also be kept at its minimum, to reduce the sample amount. The other big advantage of operating in frequency domain is that every signal processing operation, like convolutions and delays, are transformed into multiplications of arrays, which are very efficient.

There is still another optimization in how the signal is generated. Even though the signal is supposed to be at RF, the actual signal is generated in baseband and it represents the complex envelope of the signal. The clear advantage of this is the huge reduction in sample amount that needs to be handled during every operation. Furthermore, given that the generation is performed in frequency domain, the difference between the RF signal and the baseband one is just a shift in frequency, which is an immaterial operation. Then, there is no practical difference in working with the complex envelope of the signal.

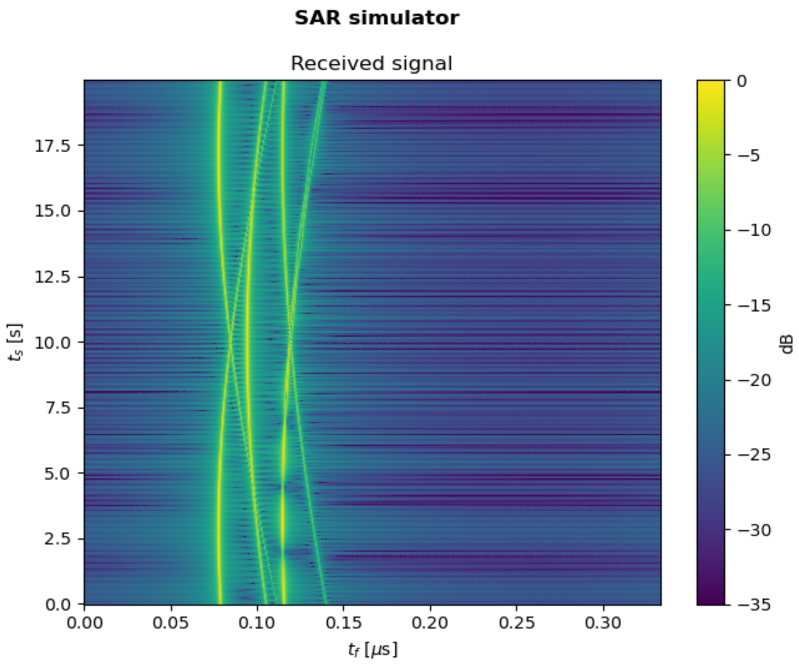

Figure 3.6 – Fast-/slow-time plot of a simulated received signal.

3.2.2 Matched filtering

The first processing step after receiving the signal, or simulating it in this case, is to filter it. The best way to do so, in terms of the output SNR, is by using a matched filter [38]. Although noise is not present in the following simulations, the matched filtering step is still included for various reasons. First thing first, noise could easily be added to the received signal, making it necessary to actually filter it. In any case, the simulator aims to be as close as possible to the hardware of an actual radar system, therefore it is important to have this step.

The matched filter function is contained, alongside all the other processing functions, in a dedicated module. The function needs as input not only the signal to which the filtering is applied, but also the signal defining the matched filter. The filter-defining signal can be passed either in time or frequency domain. The result of the filtering is the cross-correlation between the two signals, computed only in the same time interval as the received signal.

3.2.3 SAR processing

In the processing module, there are also contained the SAR processing functions. As already described in Sec. 2.6, the only way to process SAR data without any assumption over the scenario, is to implement the 3D inverse Fourier transform of the received data. This is implemented through the time-domain back-projection algorithm, which is optimized and can operate on the entire image all at once.

3.3 Simulated results of practical scenarios

Following the simulator's description, the results obtained under two scenarios are presented here. These results are meant to represent the capability of the simulator and, most importantly, to show how deep the effects of the antenna gain and scenario are on the image formation. The parameters that define the virtual radar system are based on the design of an actual radar mounted on a drone system called Dronar [10]. Similarly, the platform trajectories don't stray far off from the ones a drone typically achieve. Modern and powerful drones can fly at altitudes on the order of tens of meters to few hundreds meters. The chosen trajectories for the simulation are the ones where the platform is very close to the ground and also very close to the observed scene, in order to investigate the worst-case scenario. The simulator also needs to include a proper antenna gain to examine its effects. The gain used for the simulations has been obtained from a full-wave simulator, but the design of the simulated antenna is based on a commercial antenna being employed in the aforementioned Dronar system.

3.3.1 Simulation setup description

Two scenarios are taken into account, each meaningful for a key different aspect. The first simulation aims to recreate a scenario similar to the one encountered by classical SAR systems. The geometry of the acquisition is a linear trajectory parallel to the ground (Fig. 3.7a), with the sole difference of being much closer to the scene. Despite being similar, it will highlight the intrinsic differences that hold between the two typology of SAR systems. In the second simulation, the platform moves in a circular trajectory (Fig. 3.7b). It showcases the potential of using a drone as a platform, which is not limited to the linear trajectory. The two scenarios are each simulated twice: the first time without distortions, thus leaving only the targets' responses in the received signal, and then with both the antenna gain and path attenuation. The ideal setup serves the purpose of highlighting the effects of the close-geometry on the PSFs of the targets, meanwhile the fully distorted setup is what a real system would get and the starting point for calibration procedures. In this regard, the ideal PSF represents the goal to achieve after calibrating the SAR image and the baseline to assess the quality of a calibration method.

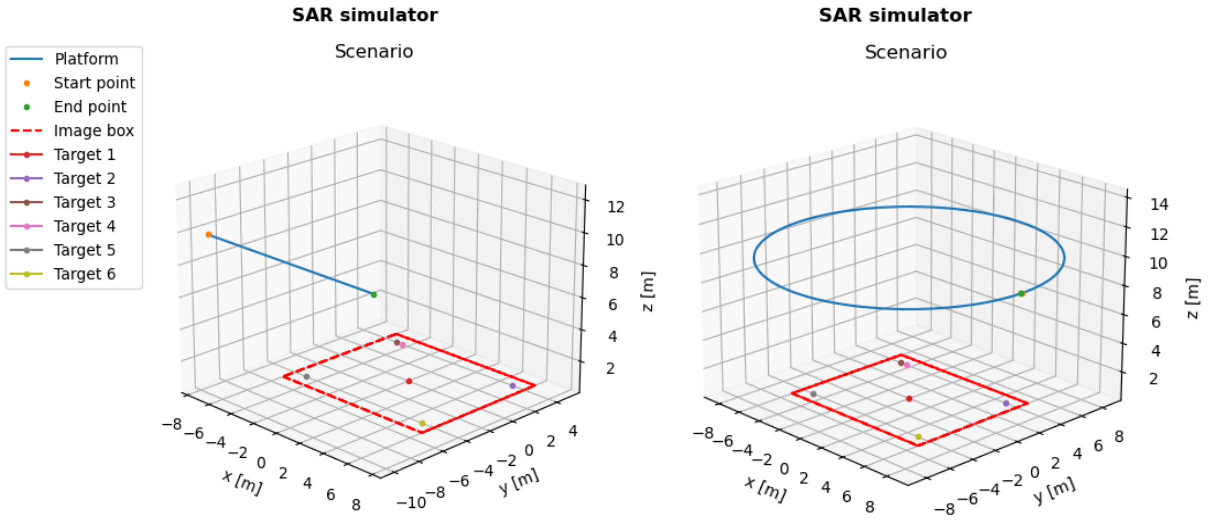

(a) **(b)**

Figure 3.7 – The trajectories of the two simulated scenarios: linear (a) and circular (b).

The simulated scenarios are described by means of a multitude of parameters. Here are presented in a summarized way the most important ones, that define the virtual radar system:

- Central operative frequency $f_0 = 2\,\mathrm{GHz}$;
- Transmitted signal bandwidth $B = 2\,\mathrm{GHz}$;
- Pulse repetition interval $T_r = 20\,\mathrm{ms}$;
- Observation interval $T_o = 20\,\mathrm{s}$.

These parameters are the same across every simulation performed. The fact that the PRI and the observation interval are also fixed, regardless of the platform trajectory, means that the spatial sampling interval will differ in the various simulations, based on how fast the platform moves. This consequence doesn't pose a problem as long as the sampling is sufficient to avoid ambiguities in the image reconstruction.

The transmitted signal is not of great interest, because the distortions it introduces are not different from the ones caused by the antenna gain, from the calibration point of view. Therefore, the signal used is a simple sinc function (Fig. 3.8), defined in frequency domain as a constant function over the bandwidth of the system.

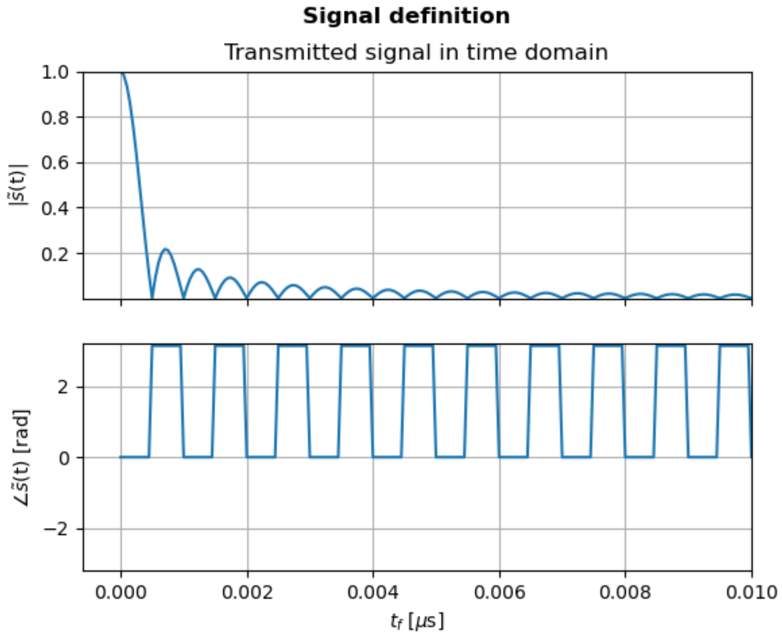

Figure 3.8 – The transmitted signal in time domain.

The targets and the image area

The choice of the targets' locations in the scene affects the effectiveness of the simulated experiments. The chosen targets disposition, shown in Fig. 3.9 and valid for both scenarios, is a selection that aims to investigate many effects at once. First and foremost, the targets are spread out in the scene, in order to assess the space variability of the PSF. Then, two targets are placed next to each other, in the platform movement direction for scenario 1, to evaluate the resolution capabilities of the system. Although the drone can easily fly in more complex configurations, providing three-dimensional images of the scene, the targets are still placed in the plane $z = 0$ and so the images are all two-dimensional. Having three-dimensional scenes would only complicate the visualizations. Lastly, the targets are chosen to have identical RCSs, in order to highlight the effects of the system alone.

All the parameters defining the targets can be found in Table 3.1.

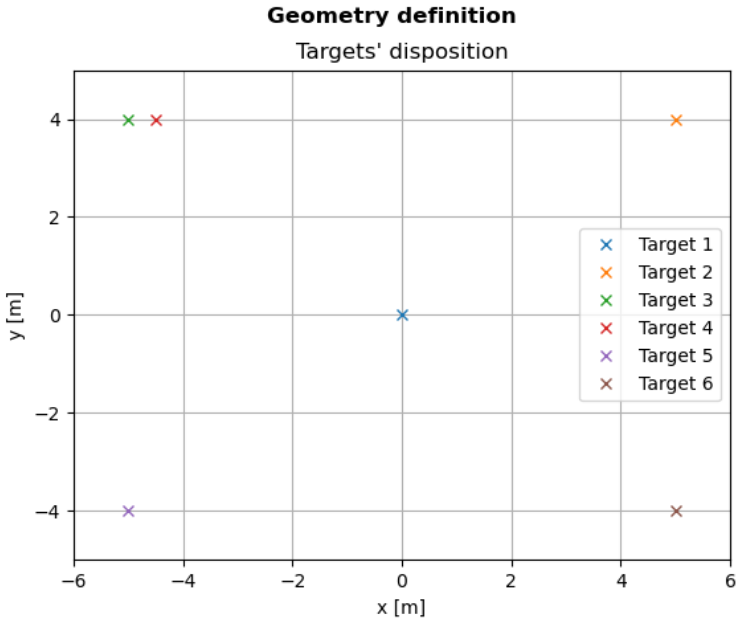

Figure 3.9 – Targets disposition for scenarios 1 and 2.

The size, location and digital resolution of the image is determined by the parameters in the system definition module. Four parameters define the boundaries of the image, declaring the lower and upper bounds for both the $x-$ and $y-$axis, while two other parameters define the digital resolutions. The image box is chosen to be tight around the targets, in order to include them and a bit of margin for the side lobes of their PSFs. The computational burden increases rapidly as the image gets bigger, so a compromise must be made between size, resolution and processing time. The digital resolution of the image would usually be chosen based on the resolution of the PSF, but since the latter is heavily depending on the acquisition geometry, that is unknown. Therefore, the digital resolution has been chosen based on the only known property: the range resolution. Given the signal bandwidth, the range resolution is $7.5\,\mathrm{cm}$, hence the digital resolution is set to be a bit smaller than this, at $5\,\mathrm{cm}$. In Table 3.2 are collected the parameters defining the image box.

The platform

The platform needs to be set up differently, based on the scenario. In scenario 1, the platform moves in a linear trajectory and doesn't need to rotate. The platform stays $10\,\mathrm{m}$ above the ground and $10\,\mathrm{m}$ away from the origin in the y coordinate. The only thing changing is the x coordinate, going from $-7\,\mathrm{m}$ to $7\,\mathrm{m}$. The antenna is pointed at the ground, in the center

Table 3.1 – Configuration summary for the targets.

	Position (x, y, z) [m]	**Reflectivity**
Target 1	$(0, 0, 0)$	1
Target 2	$(5, 4, 0)$	1
Target 3	$(-5, 4, 0)$	1
Target 4	$(-4.5, 4, 0)$	1
Target 5	$(-5, -4, 0)$	1
Target 6	$(5, -4, 0)$	1

Table 3.2 – Configuration summary for the image box.

	Start [m]	**Stop** [m]	**Resolution** [m]
$x-$**axis**	-6	6	0.05
$y-$**axis**	-5	5	0.05

region of the scene, which is also the origin of the global reference system. Fig. 3.10a shows the components of the platform position vector plotted against slow-time. In scenario 2, the platform circles around the center of the scene with a radius of 10 m, still 10 m above the ground. Since the platform is rotating relatively to the scene of interest, it must also counter rotate to compensate for the apparent rotation. The end result is the platform always facing the center of the circumference. The antenna is still pointing to the center of the scene, on the ground, but since the starting position is different, so is the orientation of the antenna. In Fig. 3.11 the trajectory and rotation history of the platform are shown. The configuration summary regarding the platform and its kinematics is given in Table 3.3.

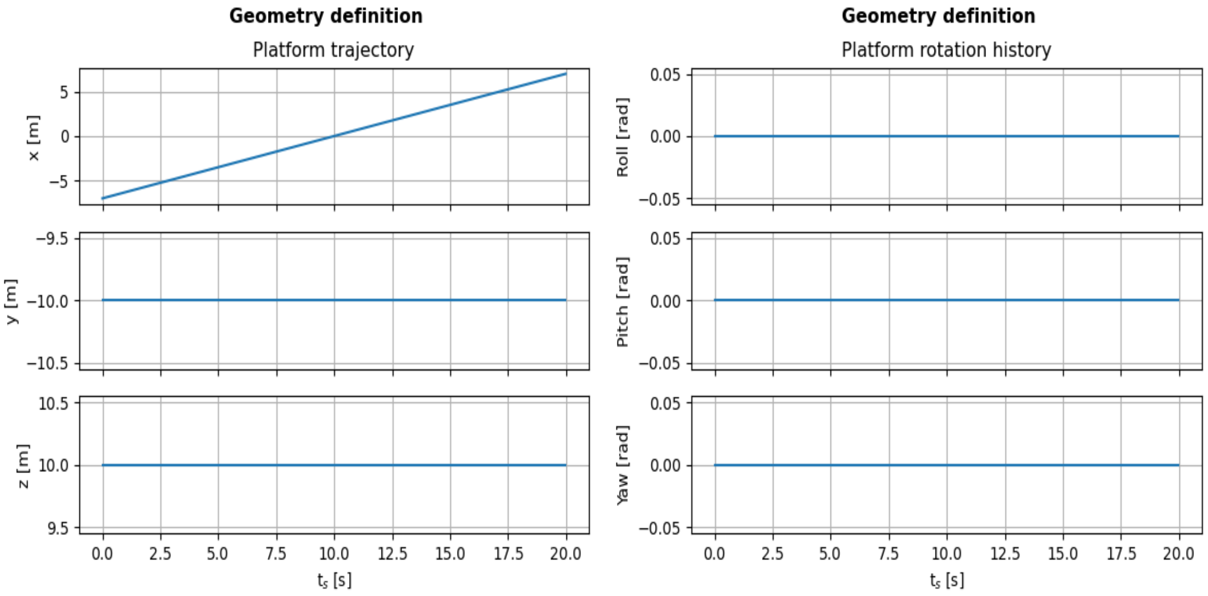

(a) (b)

Figure 3.10 – The platform trajectory (a) and rotation history (b) for scenario 1 - linear trajectory.

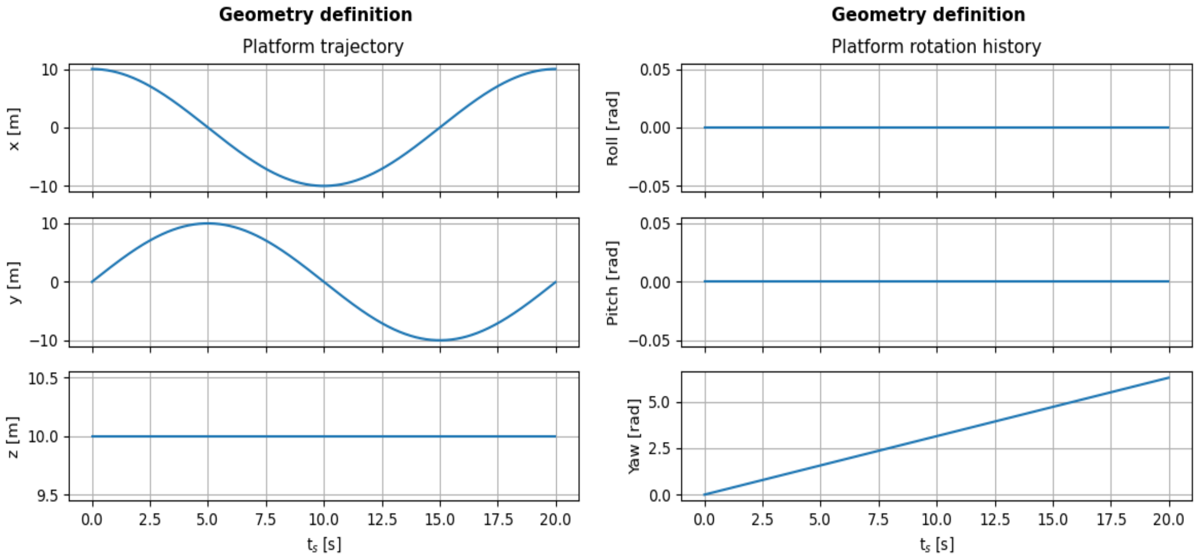

(a) **(b)**

Figure 3.11 – The platform trajectory (a) and rotation history (b) for scenario 2 - circular trajectory.

Table 3.3 – Configuration summary for the platform in the two scenarios. The parameters are: $v = 0.7$ m/s, $R = 10$ m and $\Omega = \pi/10$ rad/s.

	Trajectory (x, y, z) [m]	**Rotation history** $(roll, pitch, yaw)$ [rad]	**Antenna pointing direction** (ϕ, θ) [rad]
Scenario 1	$(vt_s - 10, -10, 10)$	$(0, 0, 0)$	$(\pi/2, 3\pi/4)$
Scenario 2	$(R\cos(\Omega t_s), R\sin(\Omega t_s), 10)$	$(0, 0, \Omega t_s)$	$(\pi, 3\pi/4)$

3.3.2 Results analysis and considerations

Linear scenario

The results from the first scenario already tell a lot about the UAV-SAR system. Even though scenario 1 is roughly a scaled down version of the classical SAR scenarios, the resulting SAR image even in the ideal case (3.12a) is completely different from what one could expect. Firstly, the PSF doesn't present orthogonal side lobes, because the distinction between range, the axis perpendicular to the platform movement direction, and cross-range, the axis parallel to the velocity vector, doesn't make sense here. In classical SAR scenarios, the viewing angles for a target in the scene are very narrow, therefore the data collection manifold is almost a rectangular surface. Then, the PSF is basically equal to a sinc in range that multiplies a sinc in cross-range. However, the close-distance scenario of Fig. 3.7a means that the viewing angles are much greater, determining a data collection manifold described by an annulus section. The PSF is thus determined by how big the annulus section is and where it is located in the spatial

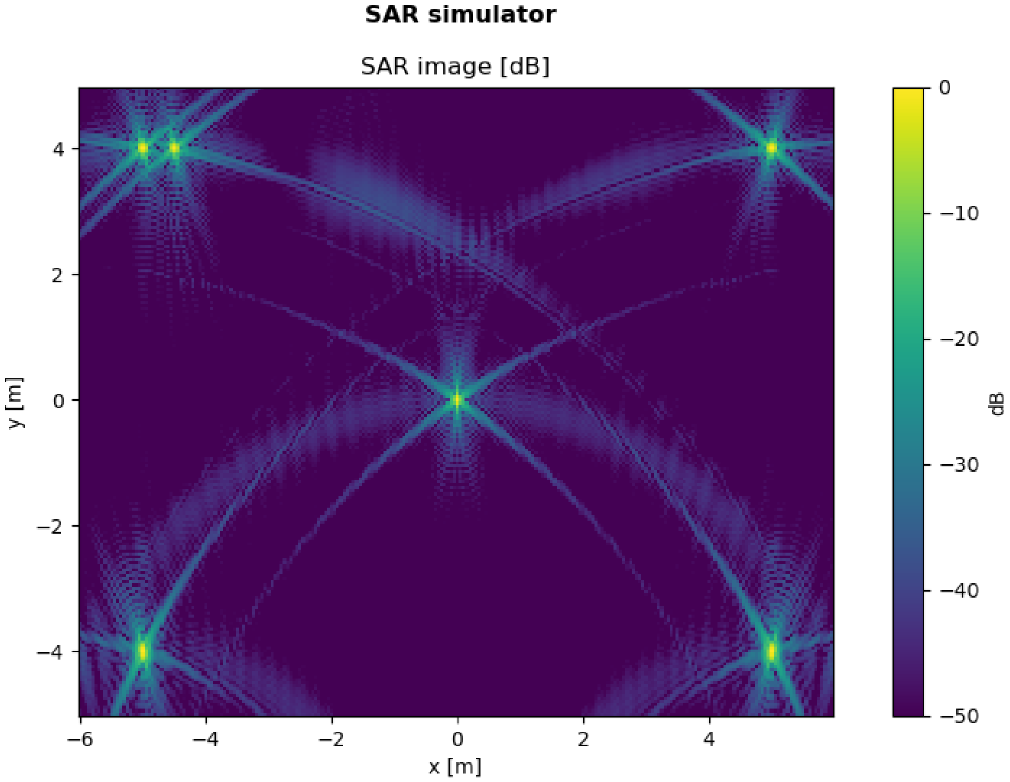

(a)

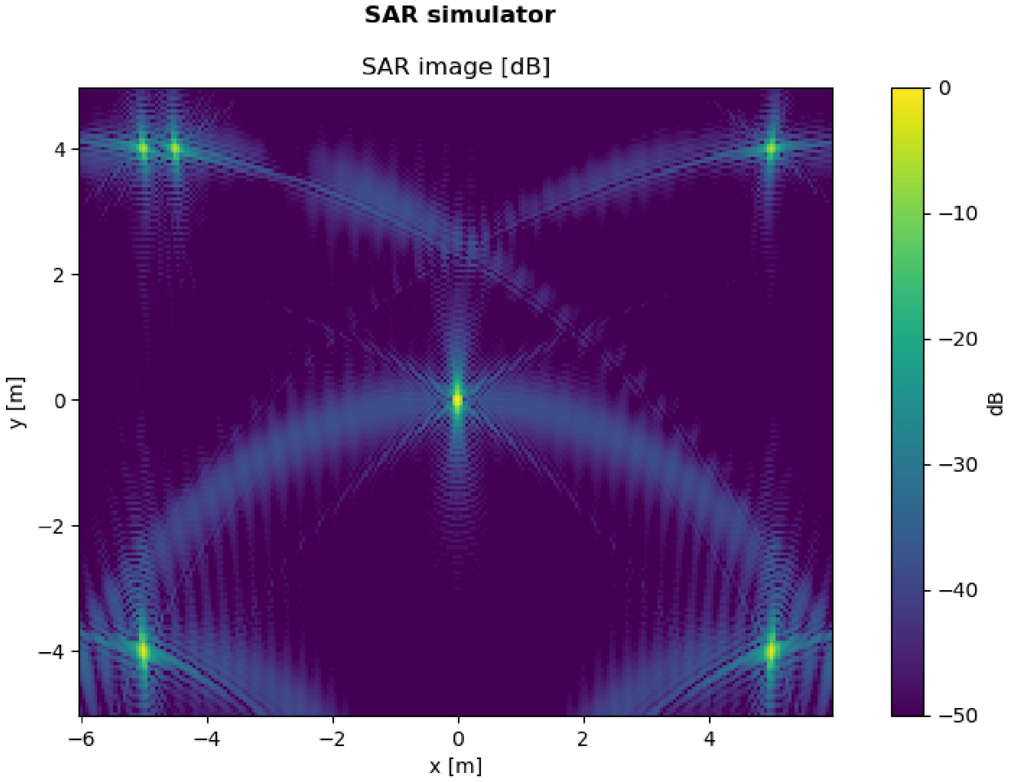

(b)

Figure 3.12 – The results obtained from the simulation of scenario 1 - linear trajectory. On the top (a), the ideal SAR image and on the bottom (b), the distorted image.

frequency domain. Since the PSF is so heavily depending on the viewing angles, it also changes very deeply from one point to the other in the image. The space variability of the PSF makes it hard to predict the properties of the image. Nonetheless, the greater the data collection manifold, the better the resolution in general. In fact, although the platform only moves for 14 m, the resolution capabilities are far greater than those of a classical SAR system. The two targets in the top-left corner of Fig. 3.12a, closer to each other, can be easily distinguished.

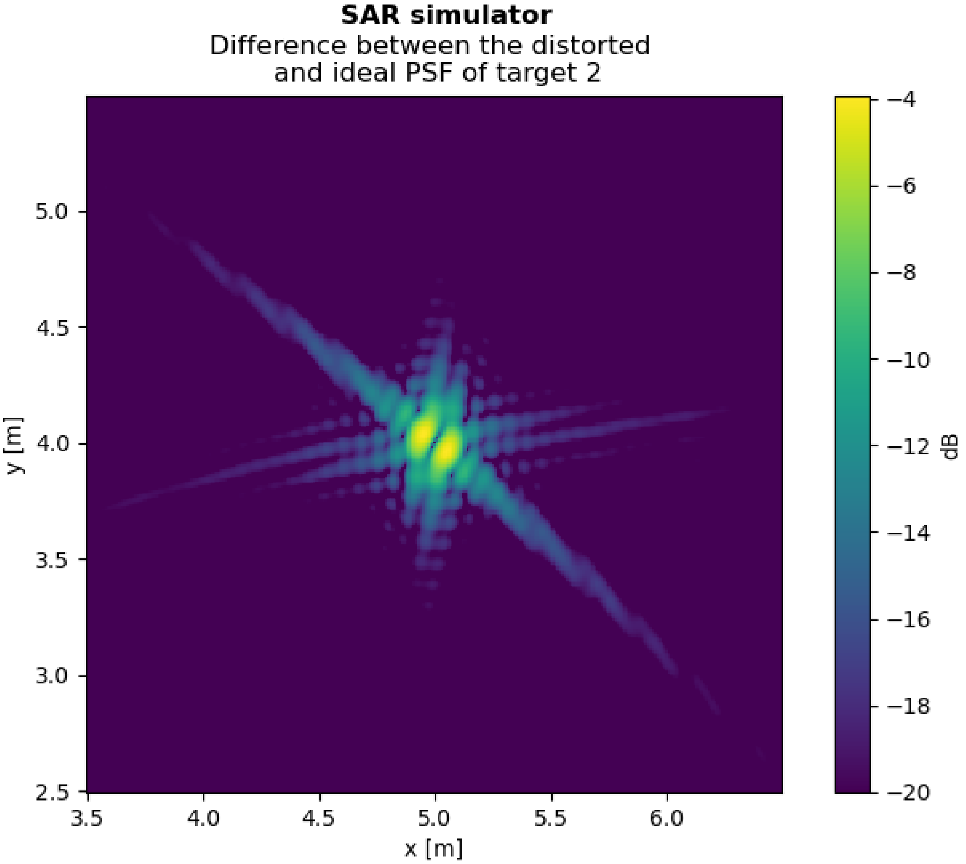

Figure 3.13 – Difference between the ideal and distorted PSFs of target 2, both normalized to their own maximum before performing the difference; scenario 1 - linear trajectory.

When it comes to the distortions, there are two major contributions that affect the PSF: the antenna gain and the path attenuation. The former depends on the looking direction and on frequency. Meanwhile, the latter solely depends on the distance between platform and target. The combined effects of the antenna gain and path attenuation are huge, and Fig. 3.13 provides a numerical example to visualize this. The image shows the difference between the PSFs of target 2, in the ideal and distorted cases, both normalized to their own maximum before performing the difference. The result is not only big in amplitude, meaning a great difference in the PSF's side lobes, but even extended in space around the target's position. Moreover, the distortions also depend on the position of the targets. To better understand these effects, it is helpful to look

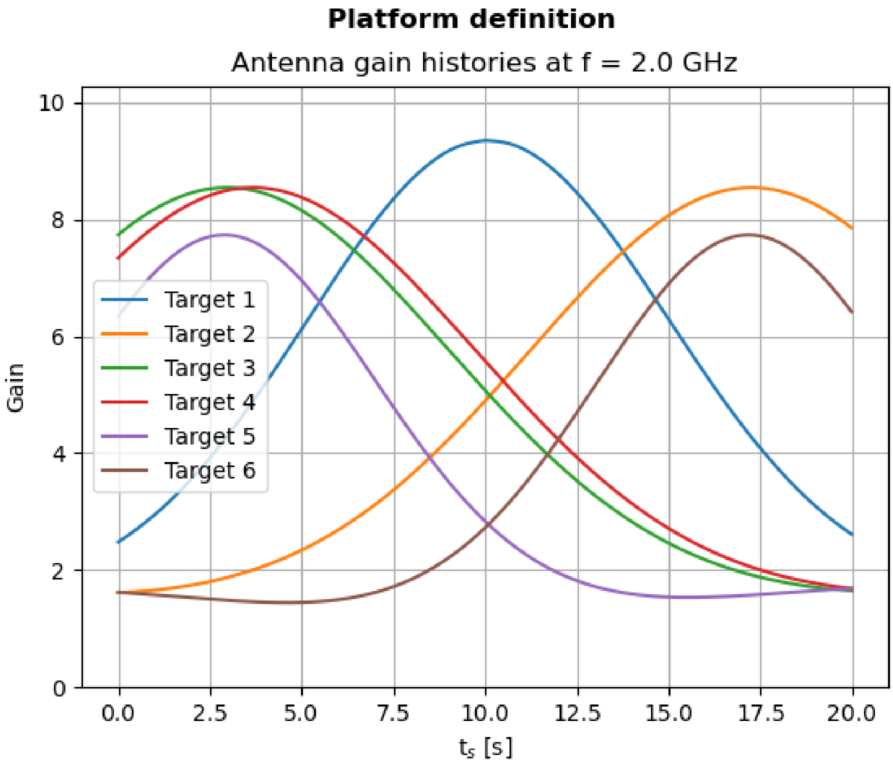

(a)

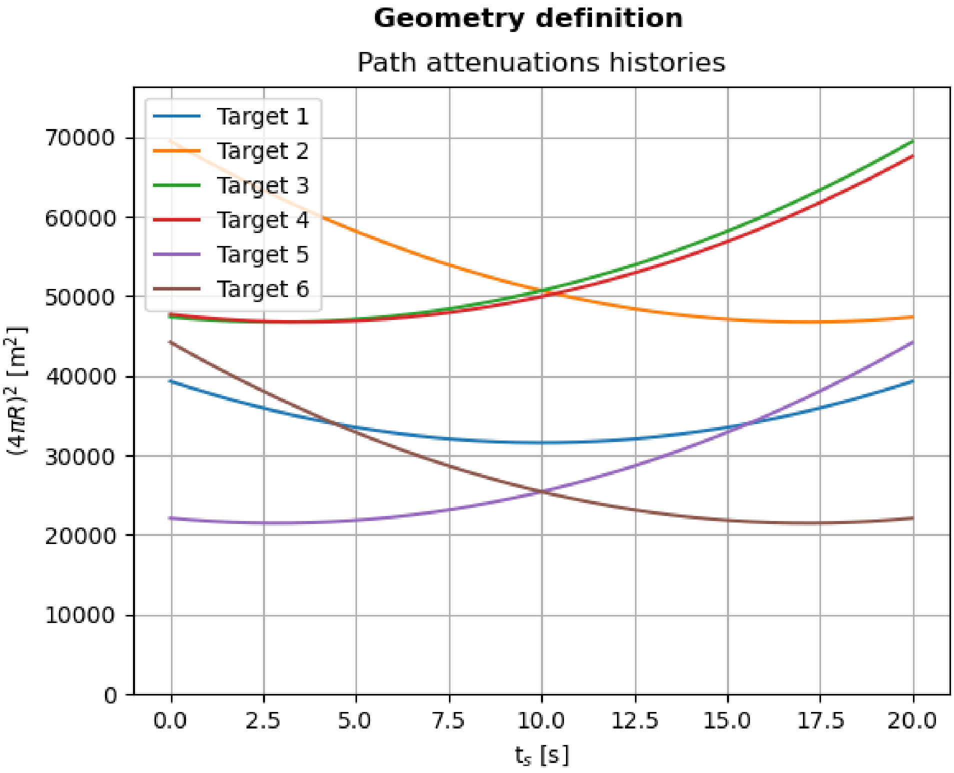

(b)

Figure 3.14 – The major distortions in scenario 1 for every target: the gain (a) and the path attenuation (a) viewed during acquisition.

at Fig. 3.14, in which the antenna gain and the path attenuation histories for each target are plotted as a function of slow-time. It can be seen that the antenna gain, at the central frequency of 2 GHz, results in a weighting function. The weighting is different for each target, but it produces a similar effect for all of them, which in this case is but a tapering of the PSF in frequency domain. The tapering results in a lowering of the side lobes and a decrease in resolution, which indeed can be clearly observed in Fig. 3.12b and it is not a controllable effect. Furthermore, the gain is also a function of frequency, hence the plots in Fig. 3.14a are only part of the weighting. The frequency dependence is shown in Fig. 3.15 for some looking directions and it is obvious that the gain is everything but uniform.

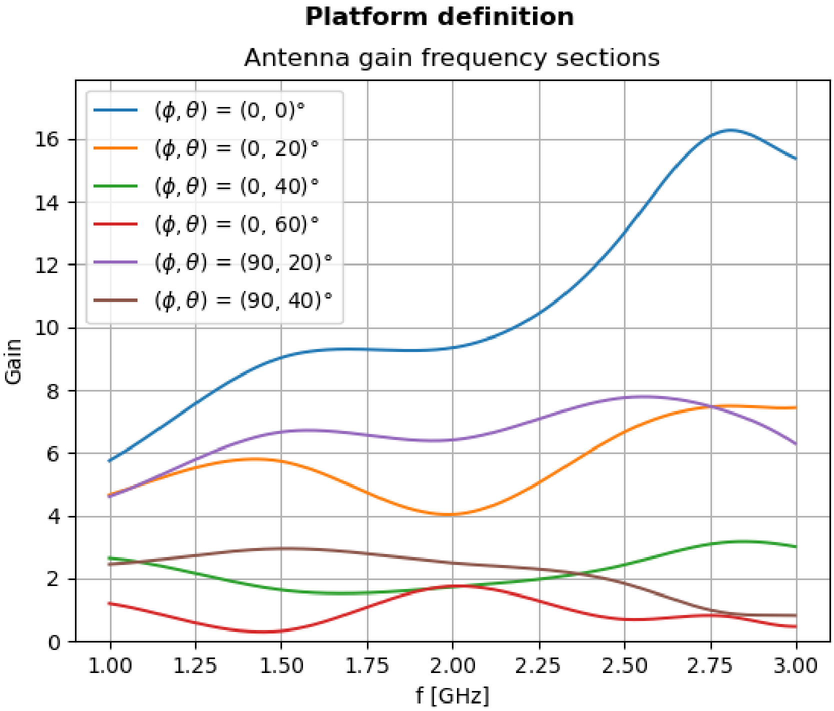

Figure 3.15 – The antenna gain as a function of frequency in various looking directions.

The path attenuation is also very problematic in the case of close-distance geometries. Usually, when the targets are far away from the platform, the path attenuation can be considered almost constant for the entire scene. In this case though, the platform is so close to the scene that two targets located apart from each other experience a different attenuation. Moreover and most importantly, the same target experiences a greatly changing path attenuation. Fig. 3.14b shows these effects for all targets. The two closest targets, namely target 5 and 6, are the ones most affected by changes in the path attenuation. This confirms the fact that the closer the geometry, the more problematic these distortions are. Indeed, their attenuation changes of a factor of 2 throughout the acquisition time.

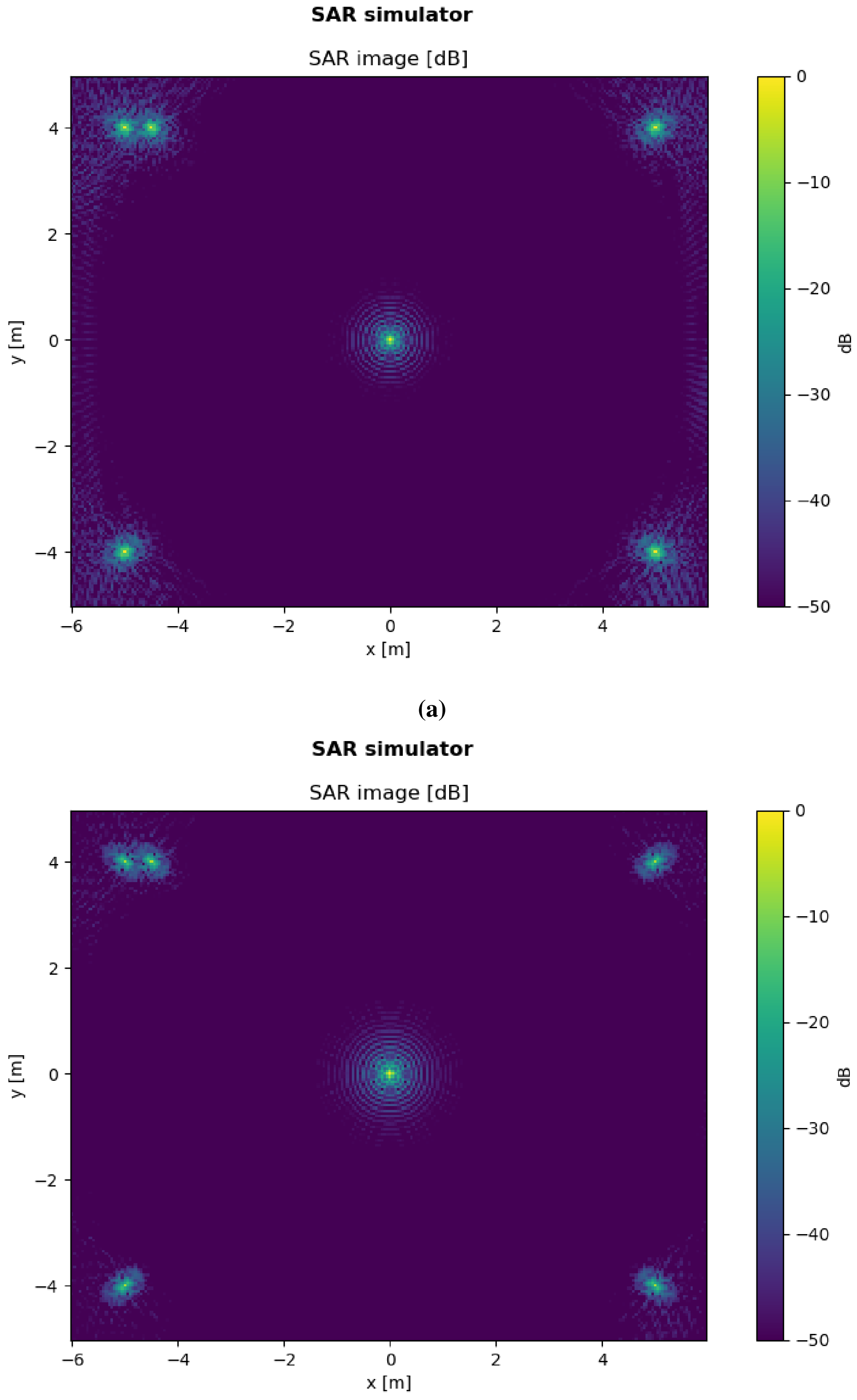

(a)

(b)

Figure 3.16 – The results obtained from the simulation of scenario 2 - circular trajectory. On the top (a), the ideal SAR image and on the bottom (b), the distorted image.

Circular scenario

Many considerations made for scenario 1 are valid also for scenario 2. Comparing the two, the difference between Fig. 3.12a and 3.16a is significant from the point of view of system performance. Just by performing a circular trajectory instead of a linear one, there is a noticeable consequence: decreasing the side lobes levels and further increasing the resolution.

In this scenario, the presence of the antenna gain affects primarily targets that are farther away from the center of the scene. In fact, as the platform flies its trajectory, the gain is pointing the center of the scene and target 1 is mostly unaffected by the gain, which nonetheless acts as a frequency filter for the transmitted signal. The same cannot be said for all the other targets, located in other positions. During its flight, the platform passes almost above them. The end result is that they are weighted by a portion of the gain that is far from the peak of the main lobe. In Fig. 3.18a, it can be seen that the gain histories for target 2 to 6 are well below the gain value seen by the first target. Looking at the distorted SAR image (Fig. 3.16b), the overall effect of this weighting is a weaker response for all targets farther away from the center.

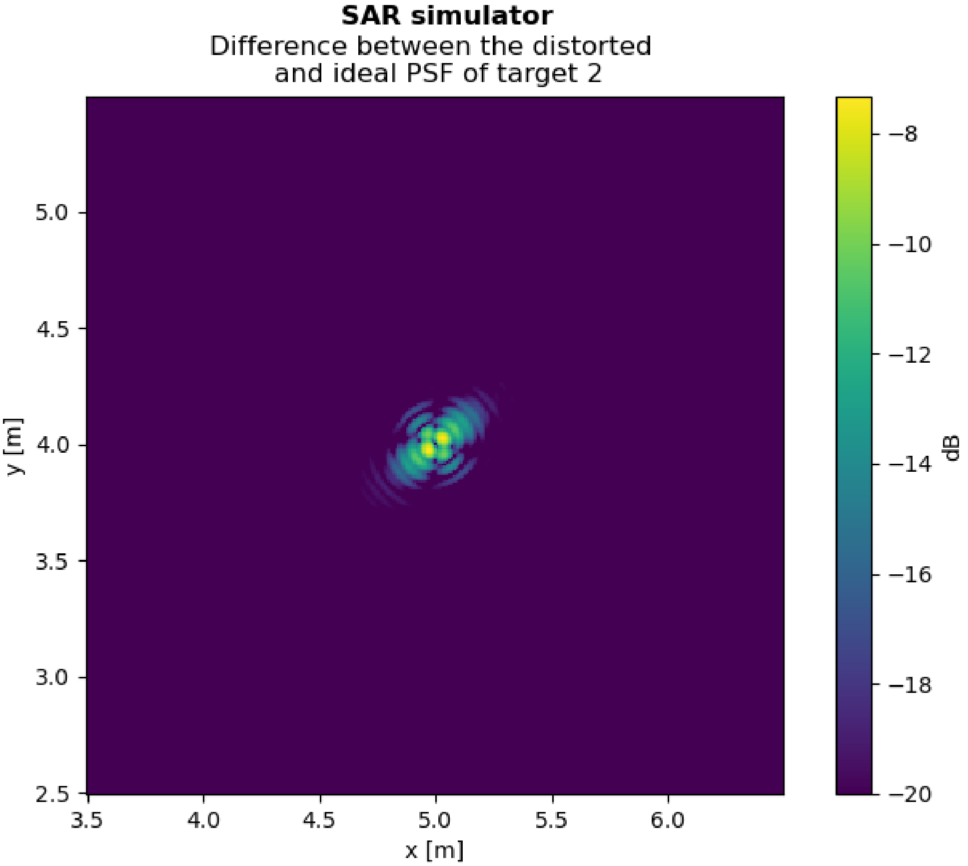

Figure 3.17 – Difference between the ideal and distorted PSFs of target 2, both normalized to their own maximum before performing the difference; scenario 2 - circular trajectory.

Furthermore, Fig. 3.18a also depicts a very dramatic situation for the other targets: the weighting functions are now much more contorted than a simple tapering. The same dramatic situation can be found in Fig. 3.18b, in which the path attenuation histories are shown. For scenario 2, the distortions rising from the path attenuation are as heavy as the ones deriving from the antenna gain. Once again, the target in the center is unaffected, because the distance from the platform is constant.

However, the increase in resolution, accompanied by the lower lobes of the PSF, make the distortions less noticeable in the final image. Computing once again the difference between the ideal and distorted PSFs (Fig. 3.17), with the same settings as before, the result is a more contained distortion and a higher peak value, meaning a smaller overall difference between the side lobes. The cause of this should probably be attributed to an averaging of the distortions terms given by the circular trajectory.

General considerations

The outcome of these two simulations already illustrates quantitatively all the problems discussed in the previous chapters. The reason of being of this thesis is then justified by the presence of these distortions, which are much more impactful than in any other SAR system.

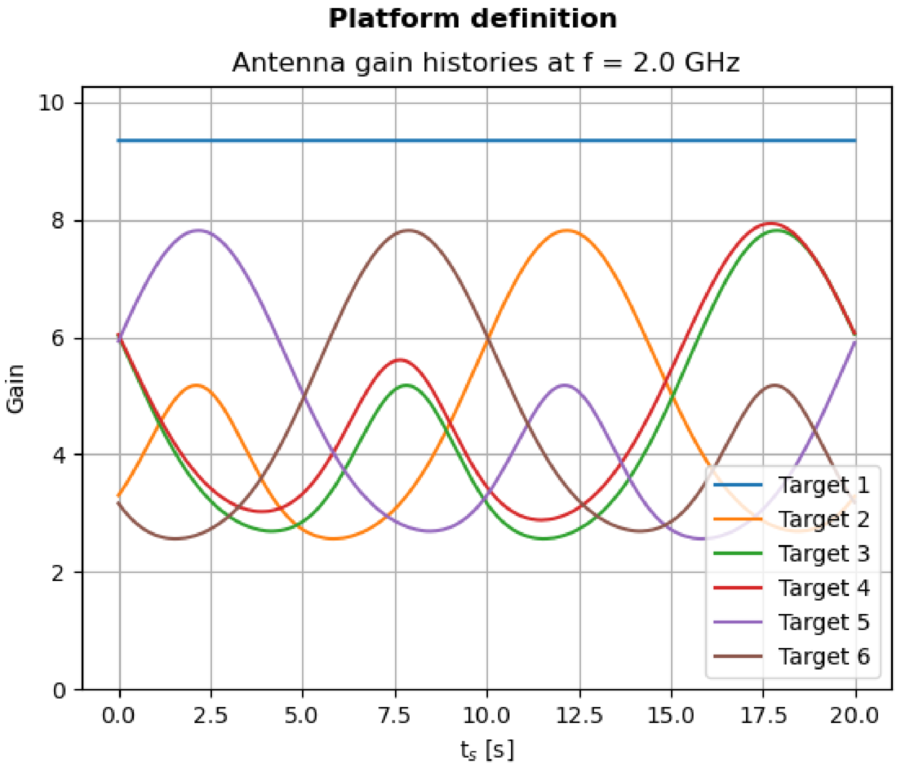

(a)

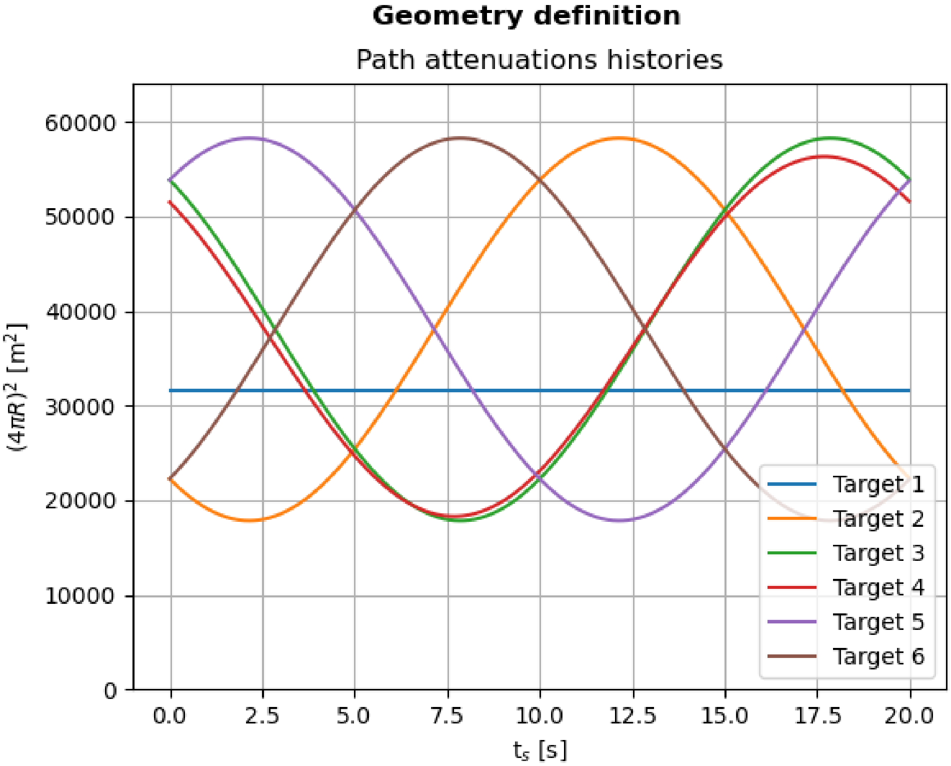

(b)

Figure 3.18 – The major distortions in scenario 2 for every target: the gain (a) and the path attenuation (a) viewed during acquisition.

Chapter 4

NUMERICAL ANALYSIS OF A STATE OF THE ART CALIBRATION METHOD

After evaluating the necessity for a more advanced calibration procedure, the initial step taken was to test a method documented in the literature. The chosen method is detailed in [39] and it was designed and implemented for the F-SAR sensor [40] at the DLR Microwave and Radar institute. This method in particular was selected because it is a validated method for the internal calibration. The results obtained through this procedure were promising and met the scientific requirements for the calibrated SAR images obtained through the F-SAR sensor. Furthermore, the method was designed taking into account the full three-dimensional geometry and the antenna gain, function of frequency and looking direction, which implies that the solution effective for the F-SAR sensor may also be applicable to UAV-SAR systems. Nonetheless, its effectiveness must be assessed for this new kind systems.

4.1 The calibration procedure

The approach described in [39] has the potential to take into account every distortion term introduced by the radar system and by the propagation path traversed by the signal. The type of calibration performed by this method is a power correction, with the goal of directly obtaining RCS measurements. Ideally, given the power SAR image, the method would return an image whose pixel values represents the RCS of the targets. In reality, the returned image is only close to the RCSs, needing a further compensation through external calibration.

The starting point to derive this procedure is the radar equation [29, Sec. 16.11] for a point-like target. Following the signal model given in Ch. 2, the radar equation can then be derived as a function of frequency:

$$P_{\mathrm{R}}(f) = \frac{|S(f)|^2 \, G^2(f, R\hat{\mathbf{i}}_0) \, \lambda^2 \, \sigma_0}{(4\pi)^3 |\mathbf{s}_0|^4}, \tag{4.1}$$

where the transmitted signal $S(f)$ is used to represent the transmitted power, G is the antenna gain, λ is the wavelength at frequency f and σ_0 is the RCS of the point-like target. This formula describes the received power just from a single acquisition. However, SAR processing produces an image by integrating all the acquisitions, over frequency and looking direction. Applying the same integration to the radar equation yields the total received power:

$$P_0 = \sigma_0 \sum_n \int_B \frac{|S(f)|^2\, G^2(f, R^{(n)}\hat{\mathbf{i}}_0^{(n)})\, \lambda^2}{(4\pi)^3 |\mathbf{s}_0^{(n)}|^4} df, \tag{4.2}$$

which adapts the integral in [39, eq. (2)]. The integration in slow-time has been substituted here by a summation over the n index, because of the discrete nature of slow-time. A lot of the terms present in the original formulation of (4.2) are irrelevant for the signal description given in this thesis. Therefore, they are assumed to be 1 to reduce the complexity and focus on the antenna and propagation related effects. The summation over slow-time is performed over the observation interval for the particular target of interest. In the simulations conducted here, every pulse is utilized to compute the SAR image, necessitating that all pulses be taken into account for calibration.

The total received power from a point-like target given in (4.2) is derived from theoretical considerations. The way this power is actually obtained from the measurements is by computing the power SAR image. Then, the total received power is given by extracting the power value in the point corresponding to where the target is located. Letting $I^2(\mathbf{x})$ be the power SAR image and assuming the target is located in $\mathbf{x}_0$, the received power is:

$$P_0 = I^2(\mathbf{x}_0). \tag{4.3}$$

Through the relationships in (4.2) and (4.3), which link together the RCS of the target, the received power and the SAR image, the method aims to reverse the relationship chain and retrieve the RCS measurement. Considering an extended target, or similarly a collection of targets (see Sec. 2.4), the operation must be performed for each pixel of the power image.

In order to do so, the integral in (4.2) has to be evaluated numerically and the power SAR image divided by the corresponding values. The previous chapter clearly proved that the distortions affecting the targets' responses differ for every point in space, therefore the integral must be evaluated individually for every spatial point in the image grid. The collection of all the evaluated integrals forms a matrix, called the calibration matrix, having the same size of the original image. The elements of the calibration matrix represent the system gain received by the corresponding pixels in the image. After dividing by the obtained calibration matrix, the calibrated power image can be considered proportional to the RCS of the targets in the scene.

4.2 Algorithm implementation

The proposed method has been implemented inside the processing module of the simulator. The function firstly computes the distortion terms that compose the integral in (4.2). Then, it proceeds to compute the calibration matrix and uses it to perform the calibration, which is a mere division of the power SAR image by the calibration matrix. At its core, the function is straightforward to implement, because the distortion terms can be obtained using the already existing objects and variables instantiated to generate the received signal.

However, a series of optimizations were implemented as part of the function itself or in addition to the bare algorithm. Firstly, the distortion terms and, consequently, the calibration matrix are computed at once time as multidimensional NumPy arrays. Thus, the integration over frequency and slow-time could be implemented using a built-in library function that operates the sum in an optimized way. In addition to this, the calibration matrix is calculated on a coarser grid, as pointed out in [39]. The extent and effectiveness of this optimization depends on how much the system gain varies from pixel to pixel. In turn, this variability depends on how small (in meters) the digital resolution is, combined with the particular acquisition geometry, the antenna gain and any other term that could eventually end up in the integral as part of the internal calibration. Hence, it is impossible to give a quantitative description of how quick the system gain varies. Nonetheless, given the average spatial resolution of the system defined in Sec. 3.3.1, which determines the digital resolution of the SAR image, it holds true that the integral can be computed on a much coarser grid of points without loss of accuracy. Lastly, there is an optimization on how the algorithm computes the calibration matrix. Given the big size of the image grid, there could be a problem storing the entire array of distortions in RAM. Therefore, the calibration matrix can be computed for a subspace of the entire image space. This block subdivision can be implemented because the algorithm is pixel-wise, i.e. it works independently on every pixel of the image.

Moreover, regardless of the acquired data, the calibration matrix can be calculated for the specific scenario, using only the information from the platform and the radar system. Consequently, the matrix could also be pre-computed or computed in parallel the SAR processing.

4.3 Calibration results

In order to investigate the applicability of the described algorithm in typical UAV-SAR scenarios, it has been tested using the scenarios presented in Sec. 3.3.1.

Linear scenario

In the first scenario, the platform follows a linear path, ensuring the antenna is consistently aimed at the scene's horizontal center line. The three targets located further from the platform's trajectory are mostly influenced by two distinct phenomena. Firstly, the antenna is never pointed with maximum antenna gain at them during the acquisitions, causing a weakening in the transmitted and received EM waves. Secondly, the greater average distance from the platform determines a greater path attenuation. The combination of the two effects results in a noticeably lower power level for these targets.

In order to confirm this intuitive reasoning, an intermediate result of the calibration process can be used as an indicator of the amount of radiometric distortions. The image in Fig. 4.1 shows the calibration matrix computed for the geometry of scenario 1, over the image grid. The plot represents in a quantitative manner the distortions introduced by the system and by the wave propagation, and it does that by associating a value to each point in space. Through this value, it is then possible to measure the average weighting experienced by a target located in the corresponding point. Thus, higher amplitude values indicate targets that will have a greater impact on the final image. On the other hand, lower amplitude values indicate apparently weaker targets.

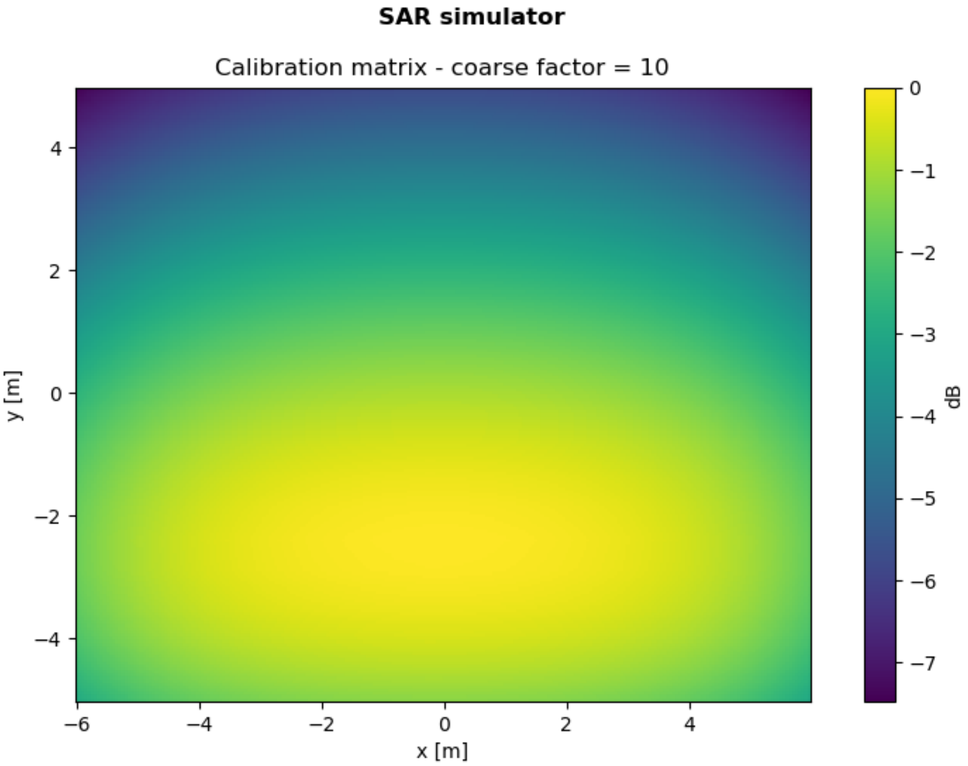

Figure 4.1 – Calibration matrix for scenario 1 - linear trajectory.

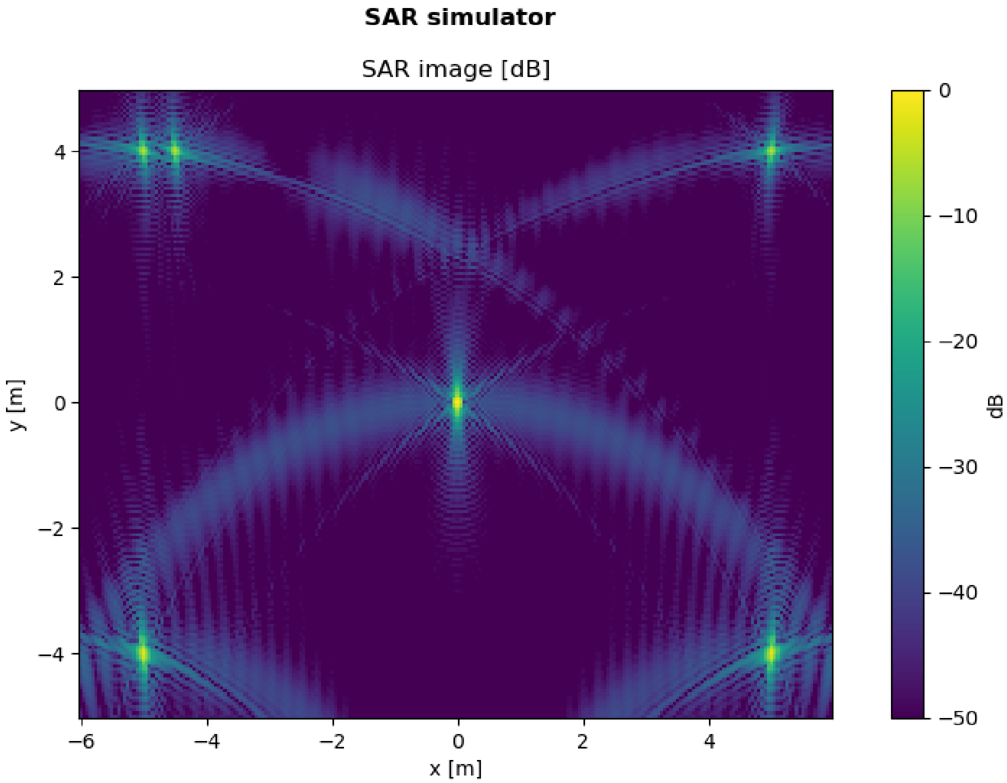

(a)

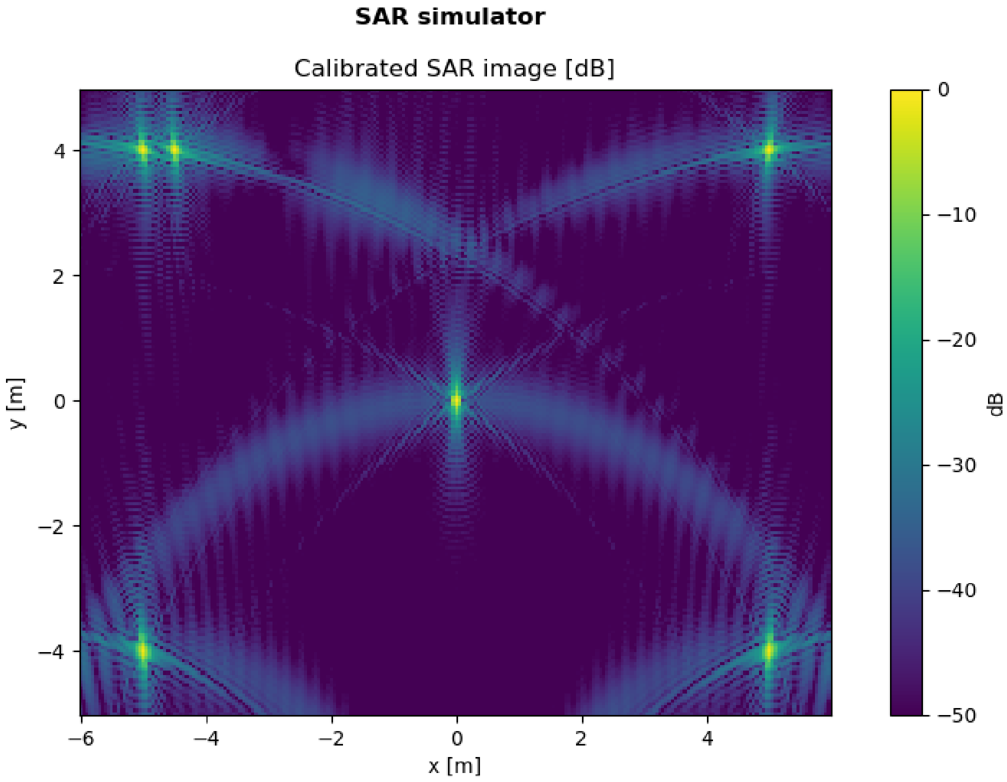

(b)

Figure 4.2 – Comparison between the uncalibrated (a) and calibrated (b) SAR images of scenario 1 - linear trajectory.

According to what has been predicted, the targets that count less are indeed the ones in the top of the image, farther away from the platform. The calibration matrix visualized in Fig. 4.1 is mainly influenced by the path attenuation, but a slight upwards shift of the peak values can be noticed, due to the antenna gain having its maximum pointed at the center of the scene. On the technical side, the matrix has been obtained with a coarse factor of 10, meaning only $1\,\%$ of the samples were computed. The factor was empirically decided based on various simulations, ensuring that the calibration values were still precise enough.

The calibrated image for scenario 1 is shown in Fig. 4.2b and is compared to the uncalibrated version (Fig. 4.2a), which has already been shown in the previous chapter (Fig. 3.12b) and is presented here again to facilitate comparison. The calibrated image clearly shows a correction on the amplitudes of the targets, especially the ones at the top of the image, that brings them all to have roughly the same power level as they should have according to the original input scene. However, the effects of the antenna gain and path attenuation on the PSFs are not limited to a modification of the power level, and the algorithm appears to do nothing in this regard. A more comprehensive discussion on this issue will be presented in the following chapter.

Circular scenario

Concerning the calibration matrix, scenario 2 may appear to be more balanced in regard to the amplitude of targets spread out across the whole image. The targets at the center have an almost constant weighting, meanwhile the off-centered targets spend equal amounts of time both far away from the platform and close to it. In fact, taking the average of each curve in Fig. 3.18b, regarding the path attenuation histories, would result in almost the same values for all targets. However, the received power is not balanced and it can be clearly seen in Fig. 4.4, where the off-centered targets are well-below the power level of target 1.

The problem lies in the combination of the path attenuation and gain weighting. When the platform is closer to a target in the corner of the scenario, the target is located underneath the antenna, which is oriented to point the center of the scene. Therefore, the lower path attenuation is compensated by the weaker gain. Vice versa, when the platform is further away from the target, the gain is higher, but there is also more distance for the EM wave to travel. This phenomenon can also be observed by overlapping the curves in Fig. 3.18a and 3.18b individually for each target.

Once again, the calibrated image (Fig. 4.3b) provides a restored power level for the off-centered targets, but the calibration procedure does not fully restore the PSFs' side lobes.

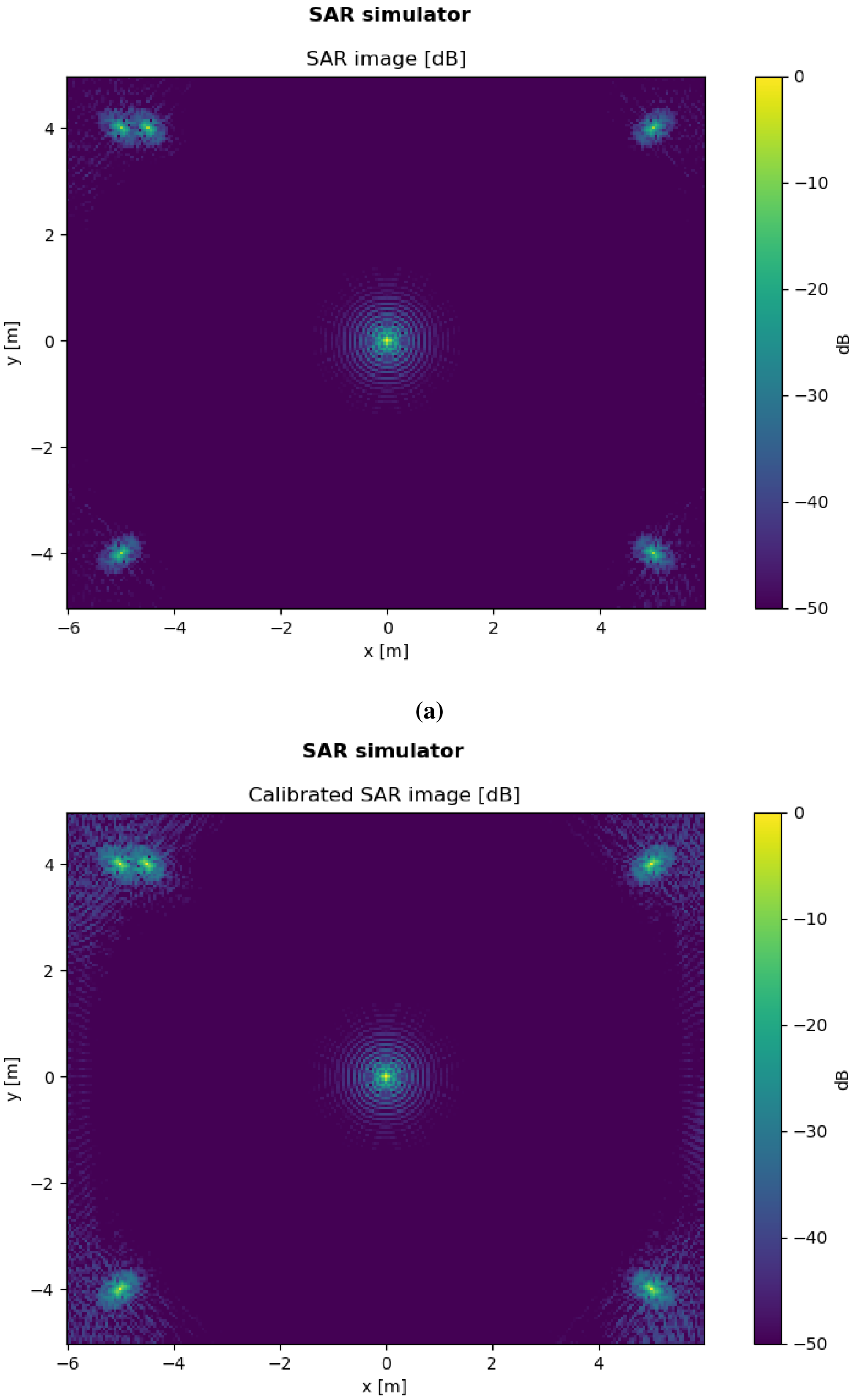

(a)

(b)

Figure 4.3 – Comparison between the uncalibrated (a) and calibrated (b) SAR images of scenario 2 - circular trajectory.

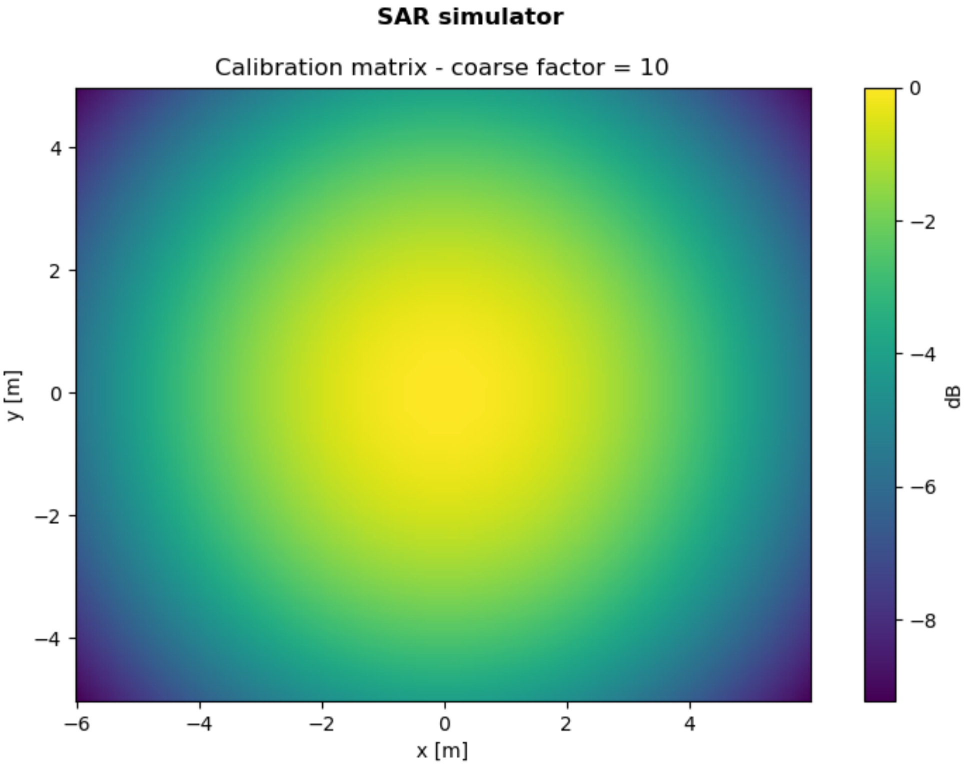

Figure 4.4 – Calibration matrix for scenario 2 - circular trajectory.

Overall performance

In order to evaluate the performance of the calibration procedure, the actual values of received power are given both for the uncalibrated and calibrated targets. Table 4.1 shows the comparison between the two versions for both scenarios.

Table 4.1 – Comparison between uncalibrated and calibrated received powers for each target. Values are normalized with respect to the first target.

	Scenario 1		**Scenario 2**	
	Uncalibrated	**Calibrated**	**Uncalibrated**	**Calibrated**
Target 1	0 dB	0 dB	0 dB	0 dB
Target 2	−5.53 dB	−0.66 dB	−6.39 dB	−0.03 dB
Target 3	−5.52 dB	−0.72 dB	−6.37 dB	−0.01 dB
Target 4	−5.16 dB	−0.59 dB	−5.62 dB	0.03 dB
Target 5	−1.77 dB	−1.37 dB	−6.39 dB	−0.03 dB
Target 6	−1.93 dB	−1.44 dB	−6.42 dB	−0.06 dB
Standard dev.	2.18 dB	0.49 dB	2.34 dB	0.03 dB

The effectiveness of the radiometric calibration is largely confirmed by comparing the standard deviations of the pre- and post-calibration received powers. After applying the calibration procedure, the power levels of the targets are brought to be almost identical to each other, which was the original setup for the simulations. Moreover, the standard deviation for both scenarios in the uncalibrated version is much lower than what it should actually be. In fact, the simulated scenarios present a biased situation: only one target is located at the center of the scene. The received powers of targets 2 to 6 are similar to each other, but they are all very different from the power of the first target. Given more targets, located at random, the pre-calibration standard deviation would have been higher, meanwhile the calibration result would have remained the same.

Chapter 5

THEORETICAL ADVANCEMENTS

The results of the previous chapter proved the calibration procedure to be very effective even for UAV-SAR systems. However, the presented method does not provide a complete correction of the images. This could be a crucial point for some applications, in which the PSF distortions could mask the actual shape of the objects. Therefore, in this chapter, the limitations of the studied method are analyzed, drawing a line on the procedure's applicability extent. Then, a more in-depth analysis of the problem itself is carried out, in order to understand more on the nature of distortions. In light of this analysis, two solutions are finally proposed to break free of the limitations of the current method.

5.1 Limitations of the proposed calibration procedure

The calibration procedure described by Marc in [39] is actually composed of two distinct calibration methods: a radiometric one and a phase calibration. It follows that the radiometric calibration was designed not taking into account the phase distortions; a distinct procedure was created for that. Indeed, the radiometric calibration operates on the power SAR image, in which the phase information is already lost. This approach leads to the limitation of having either a power-calibrated image or a phase-calibrated one, but not both at the same time. In other words, it cannot obtain an image whose amplitude represents the complex target response.

Another limitation is represented by the way the radiometric calibration procedure was developed in the first place. Starting from the radar equation, everything is thought as if only one target was present, but that is never the case. In presence of multiple targets, the SAR image is influenced in each pixel by every target. In fact, the PSFs extend indefinitely into space and the peak of one target is influenced by the side lobes of all the other targets. Nonetheless, this is not a practical limitation in most cases, because the system gain changes slowly through space. This result has been highlighted in last chapter when showing the calibration matrices for the two representative scenarios.

Two approximations can explain why the calibration method still manages to work even though its derivation is missing the contributions of multiple targets. Focusing on a target located in a particular position, its value in the SAR image is influenced by the contributions of other targets, which can be divided into two groups. The first group is represented by the nearby targets, whose side lobes contribute the most to distort the pixel value relative to the target of interest. Although their contribution is large, they experience a very similar system gain, thus the calibration matrix assigns them a comparable value. Thanks to this, the side lobes of nearby targets, which wouldn't be re-scaled by the correct amount, are still corrected with a good enough value. The same is not valid for the second group of contributors, given by the more distant targets. However, these targets are indeed further away and give a less overall contribution. Nevertheless, the issue may be more significant with targets that are neither too close nor too distant and possibly even more reflective than the target taken into consideration.

Lastly, the main limitation concerning this procedure is inherent in its working principle. The method calibrates each pixel individually, in order to bring its power as close as possible to the RCS of the target in it contained. As already explained, the method ignores the presence of the other targets' contributions that are summed to the value of a pixel. Seen from another point of view, this means that the method ignores altogether the side lobes of the PSF of every target, focusing only on its peak value. Then, the algorithm lacks the ability to properly correct for the distortions of the entire PSF. The images in Fig. 5.1 prove this claim by showing the numerical results from the simulations. Each image shows a one-dimensional cut of the normalized PSF for one target, obtained in different ways. The uncalibrated and calibrated PSFs are obtained from the same data, affected by all distortions and then calibrated through the procedure in [39], meanwhile the ideal PSF represents just the windowing function over the data collection manifold:

$$H(\mathbf{k}) = \begin{cases} 1 & \text{if } \mathbf{k} \in \text{Data collection manifold} \\ 0 & \text{otherwise} \end{cases} . \tag{5.1}$$

Comparing the normalized PSFs, it is evident how the procedure only adjusts the amplitude of the power image, but does nothing to adjust the distortions of the side lobes. The normalized PSFs before and after calibration look almost identical, because the scaling is constant over the side lobes and the normalization brings them to the same level. Once again, this could become a serious problem with targets that have different RCSs, with the side lobes of a strong scatterer masking the PSF of another target.

In [39], the problem of image quality is indeed considered, taking into account the antenna gain as the main cause of distortions in the image formation process. For this problem, the authors propose a separate solution to be performed as a pre-processing step, but it only takes

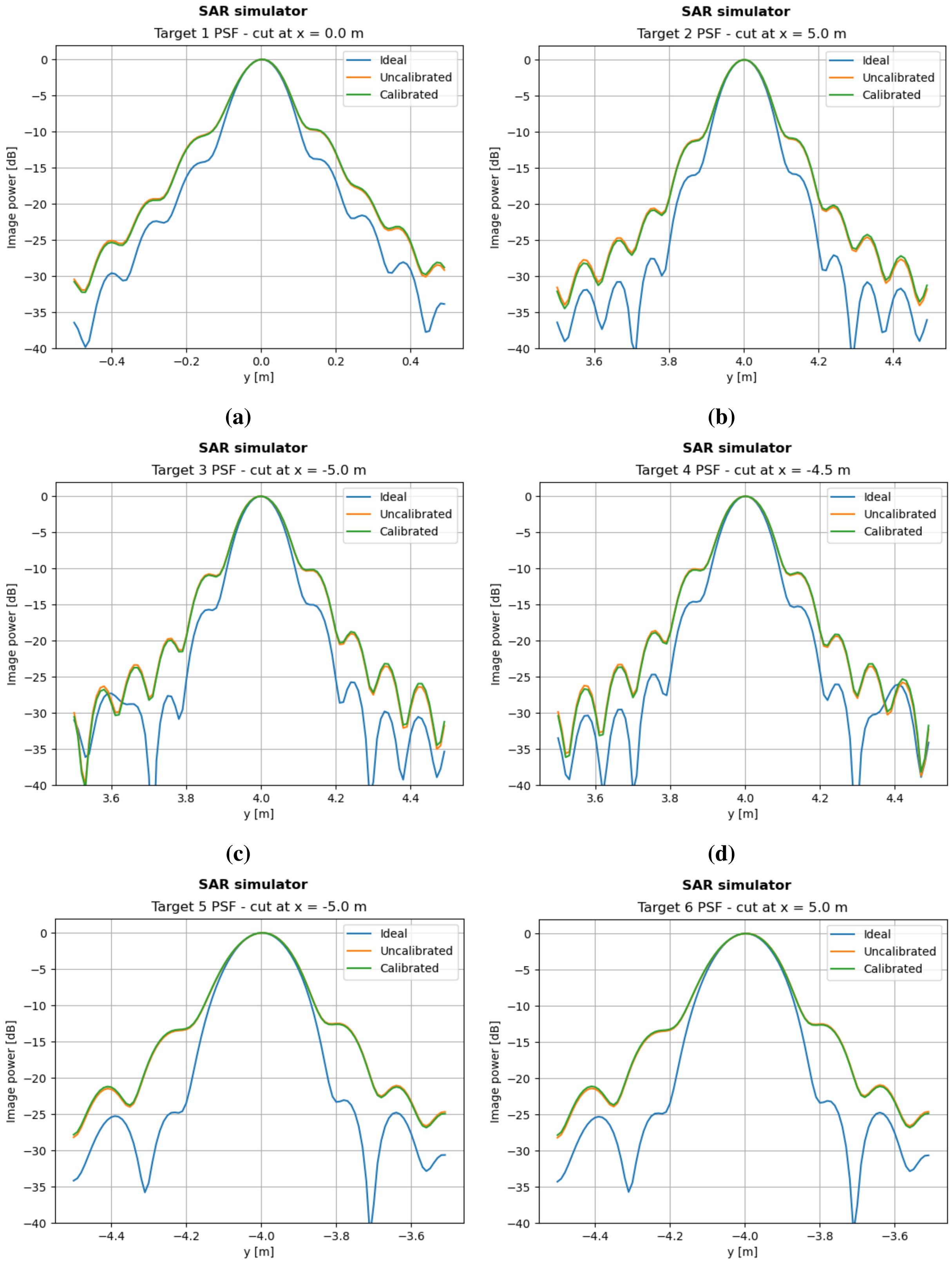

(a) **(b)**

(c) **(d)**

(e) **(f)**

Figure 5.1 – In each image, the comparison between the normalized PSFs, relative to one target, extracted from different images. Image (a) to (f) are associated to target 1 to 6, respectively.

into account the antenna gain and mainly focuses on the changes in frequency domain and elevation. Furthermore, it relies on the assumptions of a linear trajectory and a small-beamwidth antenna. As widely discussed, in UAV-SAR systems the acquisition geometry is not fixed and they are also heavily affected by the path attenuation, thus this solution would not be suited for this type of systems.

Hence, the applicability of the calibration procedure does not cover every practical scenario and caution should be exerted in choosing this method for UAV-SAR systems. The results of Ch. 4 prove that the method is very effective at calibrating SAR images, but fails to recover the distortions of the PSFs. Therefore, the method could be used in applications were only the radiometric data is needed, not the shape of the targets.

5.2 In-depth problem analysis

Some of the analyzed method's limitations are also due to the nature of the problem itself, thus a more detailed analysis of the problem is needed. In order to understand the problem with distortions and how they truly affect the image, a generic scenario must be considered. The scene is composed of multiple targets spread out in space, a platform that moves in a random trajectory and rotates during the acquisition and, mounted on the rotating platform, an antenna with a gain that is not uniform. Under these generic circumstances, the problem will be analyzed in two steps: the single acquisition case and the multiple acquisitions case.

Given a slow-time instant, the platform is in a certain location and in a certain orientation with respect to the targets. From this position and orientation, the antenna sends a pulse and receives the echoes coming from the various targets. Depending on the targets' positions, the antenna gain weighting and the path attenuation applied to the echoes will differ, thus the resulting received signal is a weighted sum of the targets' responses. The received signal can be written as follows:

$$S_{\mathrm{R}}(\omega) = \omega^2 S(\omega) \sum_j \frac{e^{-j2k|\mathbf{s}_j|}}{(4\pi|\mathbf{s}_j|)^2} G(\omega, R\hat{\mathbf{i}}_j) Q_j(2k\hat{\mathbf{i}}_j), \tag{5.2}$$

where the j index addresses the targets in the scene and $Q_j(\mathbf{k})$ is the Fourier transform of the j-th target's reflectivity function.

The ideal signal would have the distortion terms equal for every target, so that they could be brought out of the summation and corrected at once. However, this is not the case and dividing (5.2) by the distortions relative to one particular target will produce an even worse outcome.

For instance, if a target is received in the null of the antenna gain, trying to compensate for its attenuation would amplify enormously the contribution of a target in the antenna's main lobe. In the end, a single pulse cannot be used to compensate for the distortions, because it is not possible to disambiguate the received echoes from each target.

The disambiguation of the targets can be achieved with multiple acquisitions. Acquisitions from different points in space give rise to a spatial diversity in the acquired data, which can be exploited to differentiate targets in space domain. In (5.2) this is represented by the looking direction $\hat{\mathbf{i}}_j$, that determines the observed portion of $Q_j(\mathbf{k})$ and changes over the course of the acquisitions. Nonetheless, the problem discussed for the single acquisition case still persists. Through multiple acquisitions, the distortion terms change along with the useful data; a result that has already been shown in Fig. 3.14 and 3.18. The relative positions $\mathbf{s}_j$ of the targets, which in turn determine the looking directions $\hat{\mathbf{i}}_j$, shape the distortion terms as functions of slow-time. Therefore, the received signals from multiple acquisitions are also a weighted sum as in the single acquisition case, but with changing weights and changing values. This is not a new result, the collection of all the weights relative to a single target gives rise to the PSF applied to that target, and it has already been discussed that the PSF is space-variant (refer to Sec. 2.6). The combination of all received signal could be expressed in a compact way as:

$$S_{\mathrm{R}} = \sum_j H_j(\mathbf{k}_j) Q_j(\mathbf{k}_j), \tag{5.3}$$

where $H_j(\mathbf{k}_j)$ is the PSF for the j-th target, but care should be taken when summing the different targets' responses. Each target has its own data collection manifold, which depends on its location, hence $\mathbf{k}_j$ is the spatial frequency vector addressing the relative spatial frequency domain. The sum represents the superposition of the data collection manifolds associated to every target, each distorted in its own way. Once again, the compensation cannot happen for one target, because the end result would be even more distorted, and thus cannot happen for any target. Fig. 5.2 summarizes the problem in the two cases.

In order to compensate for the distortions, then, it is necessary to separate all the data collection manifolds. However, the disambiguation process, i.e. SAR processing, is impaired by the presence of the distortions and the resulting SAR image does not discriminate perfectly the targets. This is where the problem arises: in order to discriminate the various targets and perform the compensation individually, the SAR processing must be applied, but since the data collection manifolds are distorted, the result is an image already affected by the distortions, in which the targets are not well separated. Therefore, a loop is created and a perfect calibration procedure leading to the ideal PSF does not exist.

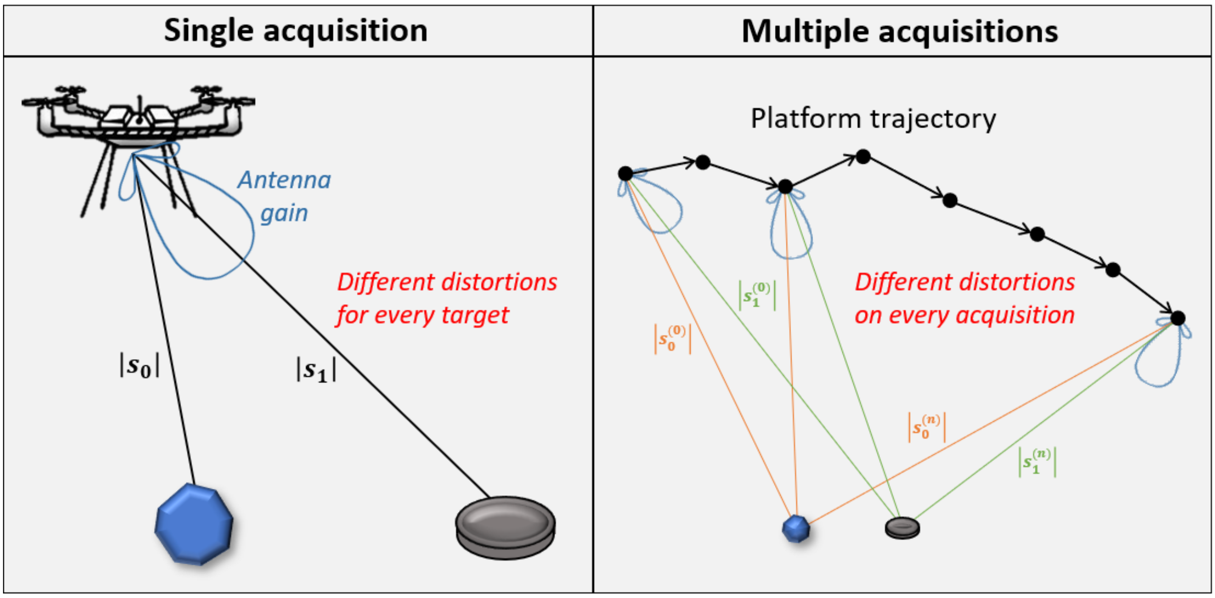

Figure 5.2 – The problem of distortions in both the single acquisition and multiple acquisition cases.

5.3 Solutions proposal: an outlook on future work

The problem is unsolvable in an exact manner, and its detailed analysis also highlighted why it is unsolvable. Hence, some assumptions can be made in order to break the loop described in the previous section. Following these assumptions, two solutions are proposed here, that could remove the distortions in the system's response function. The first of the two calibration procedures is applied as a pre-processing step, meanwhile the second operates on the already focused SAR image. Moreover, the two methods could also be combined and compensate for each other's weaknesses.

The methods discussed here provide only a theoretical framework on how the solutions would work and why, but more research is still needed. Thus, they should be considered as proposals for a future development work on the subject, and not an actual implementable algorithm. Furthermore, it is unclear how these solutions would behave in conjunction with side lobe-reducing windowing filters.

5.3.1 Beamforming

The first calibration procedure is applied directly to the received pulses, before SAR processing. It is thought to mainly compensate for the antenna gain, with the idea of discriminating the direction of arrivals (DOAs) of the targets' responses. The other distortions introduced by the system and propagation path should be calibrated in another way, for instance, and not exclusively, by using the other proposed solution.

In order to understand the idea behind this method, it is useful to analyze the SAR approach. SAR systems create a virtual array from which the pulses are received. However, the array thus formed is very large, incurring in a near-field geometry for which the targets are seen from multiple looking directions (Fig. 5.3). In other words, the rotated line of sight vector $R\hat{\mathbf{i}}$ changes greatly over the course of the acquisition. Therefore, it is not possible to define a unique looking direction for a target, which is necessary to assign a unique value of the antenna gain, and compensate for it

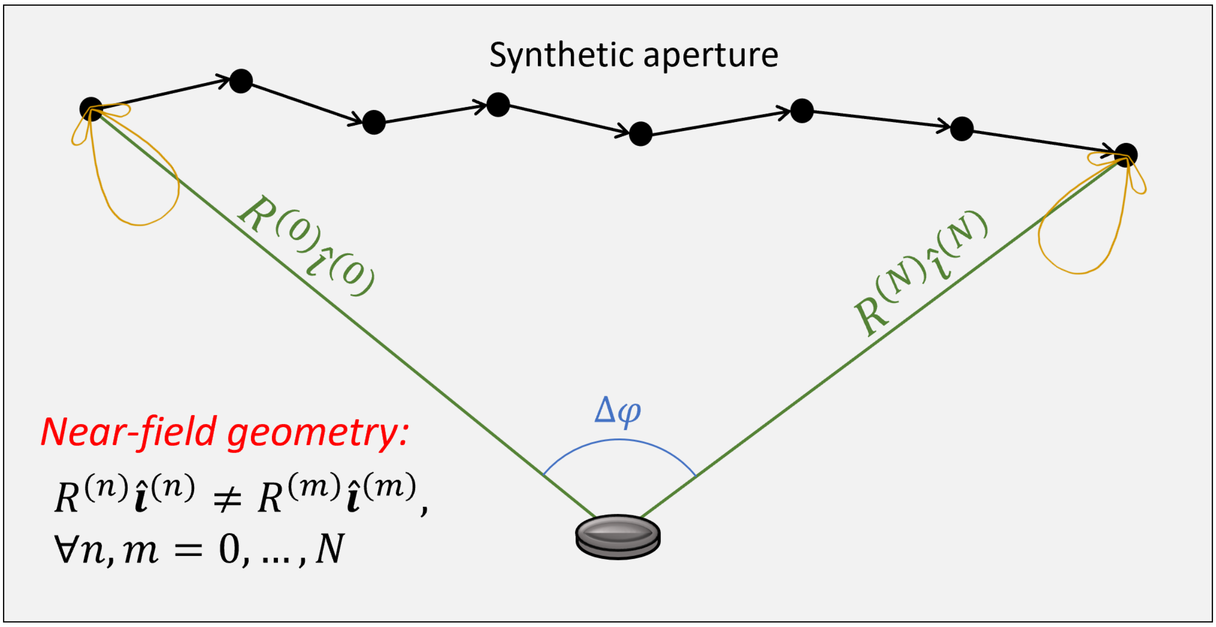

Figure 5.3 – The problem with the synthetic array formed by a SAR system: the targets are usually located in a near-field geometry.

The solution to this problem is to reduce the amount of processed pulses, and it goes against the principle of SAR. Reducing the amount of pulses means to consider only a subset of the platform's positions, which in turn translates in a smaller virtual array. With a small number of processed pulses, the resulting virtual array could be small enough to respect the far-field conditions relatively to the target. In Ch. 2, the far-field condition was supposed to be true for the physical antenna, and the approximation was applied to the target. Here, the approximation is given for granted for both the target and the physical antenna, and it is being applied again to the virtual array. The conditions that must hold for the far-field approximation to be true are now reversed, because it is the array that must adapt to the scene. The conditions [29, eq. (15.7.3)] become:

$$L << D \quad \text{and} \quad L << \sqrt{\lambda_{min} D/2}, \tag{5.4}$$

where L is the array's total size, D is the distance from the array's phase center and the closest target in the scene and λ_{min} is the smallest wavelength in the transmitted EM wave. Thanks to this approach, a unique DOA exists for each target and a constant antenna gain value can be associated with it. In mathematical terms, the rotated line of sight vector is approximately constant for N acquisition:

$$R^{(n)}\hat{\mathbf{i}}^{(n)} \approx R^{(m)}\hat{\mathbf{i}}^{(m)}, \quad \forall\, n, m = 0, \ldots, N. \tag{5.5}$$

Therefore, the antenna gain value $G(\omega, R^{(n)}\hat{\mathbf{i}}^{(n)})$ is also approximately constant for N acquisition, as illustrated in Fig. 5.4

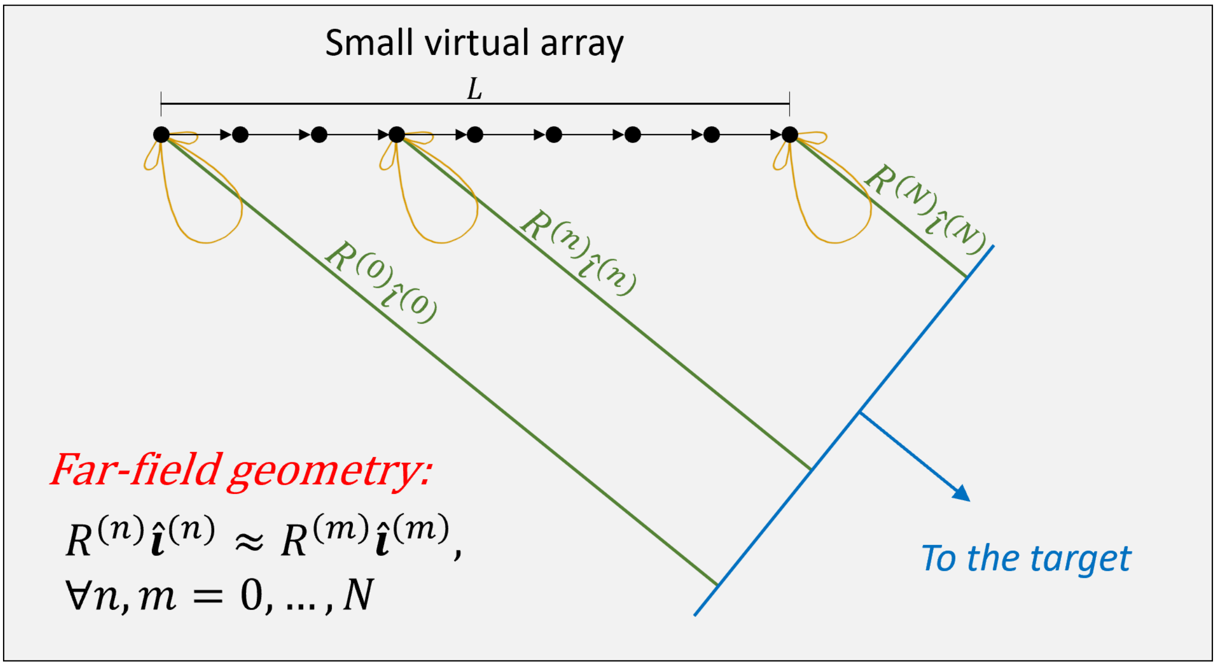

Figure 5.4 – A small virtual array formed by a limited number of received signal. The far-field conditions are verified and a unique DOA exists for a target.

The small virtual array is thus suitable to undergo beamforming processing, that enables to discriminate the DOA of all the targets simultaneously. After applying a beamforming algorithm, the slow-/fast-time matrix of received pulses gets transformed into a DOA/fast-time matrix, in which each fast-time pulse is associated to a looking direction. Since the gain is also a function of frequency, the fast-time pulses must first be transformed into frequency domain, and then the actual compensation can take place. The frequency domain pulses can finally be divided by the antenna gain function in the corresponding directions. Afterwards, the method proceeds to transform back the compensated DOA/fast-time matrix into the slow-/fast-time matrix of pulses. The resulting matrix of received pulses differs from the starting matrix in that the signals are received as if an isotropic antenna was mounted on the platform. The advantage of reintegrating the DOAs into slow-time is that it allows the subsequent SAR processing to remain unchanged. The same procedure is then replicated for every consecutive batch of received pulses, so that every virtual array is in far-field conditions.

The downside of this calibration procedure is that its effectiveness strongly depends on the acquisition geometry. The number of computed DOAs can be decided arbitrarily when applying beamforming processing, but the angular resolution is still limited by the physical size of the virtual array and by the specific beamforming algorithm. More advanced algorithms exploit the statistical information between the signals received from each array element (in this case, the platform's positions). Therefore, they compensate the limited spatial diversity given by the small number of processed pulses. Nonetheless, the physical size of the virtual array is determined, at its maximum, by the geometry: the closer the targets, the smaller the array. Hence, the angular resolution is not controllable and it could be too rough to operate an effective compensation. Furthermore, the beamforming processor has also to cope with high-bandwidth signals.

5.3.2 Batch processing of distortions

The second calibration procedure tries to break the loop after the targets have been imperfectly discriminated. The method operates on the SAR image assuming that the targets have been discriminated with a certain degree of separation. Considering a small volume within the scene, the targets in it contained are not well separated from each other, but they are separated well enough from the further away targets to neglect their presence. In addition to this, another assumption can be made for these targets, which is the foundation of the method. Looking at the calibration matrices shown in the previous chapter, they prove that the distortions change slowly as a function of space. Although the calibration matrix represents the system gain and not the distortion terms themselves, a similar behavior can be expected for the latter. Hence, the assumption made is to consider the distortions as constant across the small volume. Furthermore, by adjusting the size of the volume, the assumption is guaranteed to be true. Fig. 5.5 depicts the concept: a small volume will have roughly the same path attenuation and the same antenna gain value associated with all the inner points.

Then, the method considers a block of the image, corresponding to the small volume, and transforms it into spatial frequency domain, computing the available points of the data collection manifold. The outcome of this operation is equal to the collection of all received signals coming from the considered volume. Under the approximations described above, the resulting Fourier

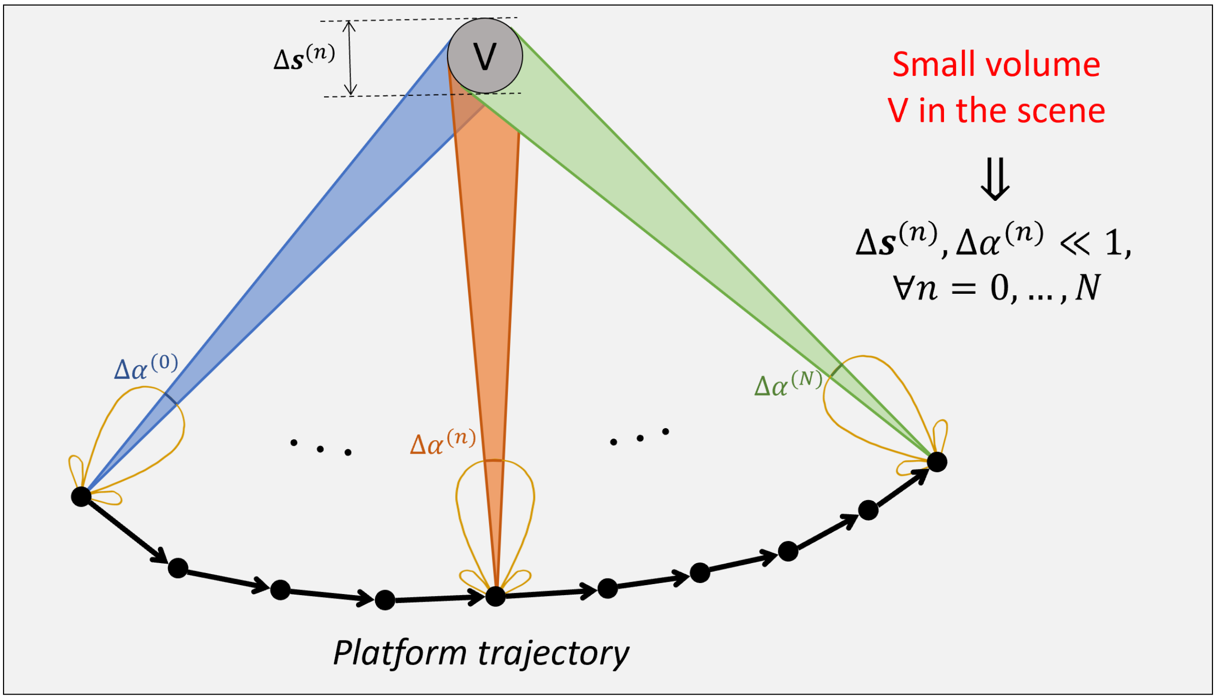

Figure 5.5 – Approximately, the targets within a small volume will experience the same distortions for every acquisition.

transform can be approximated as:

$$S_{\mathrm{R}} = \sum_j H_j(\mathbf{k}_j)Q_j(\mathbf{k}_j) \approx H(\mathbf{k}) \sum_j Q_j(\mathbf{k}), \tag{5.6}$$

where j is limited to the targets in the volume. Additionally, the spatial frequency vectors $\mathbf{k}_j$ coincide for the targets in the volume, because the viewing angles are very similar and so are the data collection manifolds. Consequently, the calibration can be performed simultaneously for all targets within the volume, dividing by the distortion function $H(\mathbf{k})$. In order to reduce the approximation error, the method should use the distortion function experienced by a target in the volume's center. Finally, once the calibration procedure is completed, the data can be transformed back into space domain and put in place of the original portion in the SAR image.

This method is relatable to the procedure described in [39], as they both operate on the SAR image's pixels and rely on the slow variability of the distortions. However, while the tested procedure operates on the pixels individually, this novel solution operates on the whole PSF, thus addressing the problem of the side lobes distortions. Therefore, the resulting SAR image is, ideally, both radiometrically correct and distortion-free. Furthermore, nothing prevents to use the full complex antenna field radiation pattern, and any other phase contribution introduced by the system, to calibrate the target's responses. This approach would then lead to an all-in-one solution to fully calibrate the UAV-SAR system.

CONCLUSIONS

The development of calibration procedures for SAR systems has long captivated the scientific community. Calibrated SAR images allow to do more than just analyze visually the content of the observed scene, they enable to process quantitatively the data in the images to obtain higher-level results. Air- and spaceborne SAR systems exist ever since the 1950s, therefore many procedures have been proposed, tested and validated for them. However, the birth of a new kind of SAR system, the drone-borne systems, posed once again the challenge of finding an effective and validated calibration procedure that could correct the distortions in the system's response function.

Calibration procedures divide into two main branches: internal and external calibration methods. In air- and spaceborne systems, internal calibration usually compensates for the distortions introduced by the radar's components and some propagation effects, offloading to external calibration the compensation for the antenna gain and every other imperfection of the system model. In UAV-SAR systems, the scenario is completely different, with high-bandwidth transmitted signals, high-beamwidth antennas and arbitrary flight trajectories just tens of meters from the observed scene. Hence, an advanced internal calibration procedure is required for this kind of systems, accounting for the three-dimensional acquisition geometry and the full antenna gain as a function of frequency and looking direction.

Ch. 3 describes the SAR simulator that has been created specifically to cope with UAV-SAR systems. Specifically, the simulator can generate received signals in the manner a generic SAR system would produce, without limitations on the radar system's parameters, the antenna type and orientation, the acquisition geometry and the targets' positions. The SAR images obtained from simulating two representative scenarios, typical for drone-borne systems, showed the inherent differences between the classic air- and spaceborne's acquisition geometries and the newer close-distance geometries. Furthermore, by simulating equal-power targets, the results showed the extents of the distortions caused by the antenna gain and the changing path attenuation, proving the need for a powerful calibration procedure.

The method in [39] was developed for an airborne system and validated with experimental data, that, once calibrated, met the scientific requirement for that system. Moreover, the method tries to compensate for the full three-dimensional antenna gain, the propagation effects and every other distortion term present in the received signal, because the system for which it was developed has more similarities with a drone-borne system than a spaceborne one. Therefore, the same method was investigated in Ch. 4 for the two scenarios presented in Sec. 3.3.1. The outcome of the calibration procedure is a power image that shows similar levels for all targets, re-scaling the attenuated PSFs. The improvement is quantitatively proved by computing the standard deviations of the peak values for the six targets, before and after calibration. The standard deviation gets reduced in both scenarios by a conspicuous factor, bringing it to 0.49 dB in the linear trajectory scenario and to almost 0 dB for the circular trajectory scenario. Such result is promising, but it doesn't give the full picture. Analyzing the entire PSF for each target, it is clear how the method only operates a constant re-scaling of the power level, leaving the side lobes still distorted. Hence, the use of this method is suggested only for applications in which the shape of the objects in the scene is not of great interest, or in high-resolution SAR images, where the PSFs' side lobes are mostly unaffected by the distortions.

In conclusion, the limitations of the existing methods push the search for a new calibration procedure to be adopted for UAV-SAR systems. A more in-depth analysis of the problem led to discover two innovative theoretical solutions, that could overcome the limitations. Especially in regard to the solution described in Sec. 5.3.2, the potential of this new method is to have a complete calibration procedure that could take care of the radiometric and phase distortions as well as retrieve the ideal PSF. However, more research must be done to finally come up with a usable algorithm implementing these solutions. Furthermore, more evaluation testing for the analyzed method could be conducted in a future work. The presented scenarios contained targets of equal RCS, because the interest was on system's distortions. Then, simulated scenarios with more targets, at different power level and located in other configurations could reveal the true applicability boundaries for the calibration procedure in [39]. Finally, it is mandatory to test this method on actual data obtained from a real UAV-SAR system.

REFERENCES

[1] Carl A. Wiley. “Synthetic Aperture Radars”. In: *IEEE Transactions on Aerospace and Electronic Systems* AES-21.3 (May 1985), pp. 440–443. ISSN: 1557-9603. DOI: `10.1109/TAES.1985.310578`. URL: `https://ieeexplore.ieee.org/document/4104077` (visited on 05/17/2024).

[2] Fabio Bovenga et al. “Assessing the Potential of Long, Multi-Temporal SAR Interferometry Time Series for Slope Instability Monitoring: Two Case Studies in Southern Italy”. In: *Remote Sensing* 14.7 (7 Jan. 2022), p. 1677. ISSN: 2072-4292. DOI: `10.3390/rs14071677`. URL: `https://www.mdpi.com/2072-4292/14/7/1677` (visited on 05/17/2024).

[3] Henri Riihimäki, Miska Luoto, and Janne Heiskanen. “Estimating Fractional Cover of Tundra Vegetation at Multiple Scales Using Unmanned Aerial Systems and Optical Satellite Data”. In: *Remote Sensing of Environment* 224 (Apr. 1, 2019), pp. 119–132. ISSN: 0034-4257. DOI: `10.1016/j.rse.2019.01.030`. URL: `https://www.sciencedirect.com/science/article/pii/S0034425719300367` (visited on 05/17/2024).

[4] Syed Agha Hassnain Mohsan et al. “Unmanned Aerial Vehicles (UAVs): Practical Aspects, Applications, Open Challenges, Security Issues, and Future Trends”. In: *Intelligent Service Robotics* 16.1 (Mar. 1, 2023), pp. 109–137. ISSN: 1861-2784. DOI: `10.1007/s11370-022-00452-4`. URL: `https://doi.org/10.1007/s11370-022-00452-4` (visited on 05/17/2024).

[5] Frédéric Brigui et al. “SAR-Light - First SAR Images from the New Onera SAR Sensor on UAV Platform”. In: *IGARSS 2022 - 2022 IEEE International Geoscience and Remote Sensing Symposium*. IGARSS 2022 - 2022 IEEE International Geoscience and Remote Sensing Symposium. July 2022, pp. 7721–7724. DOI: `10.1109/IGARSS46834.2022.9884340`. URL: `https://ieeexplore.ieee.org/document/9884340` (visited on 04/09/2024).

[6] Nouvel Jean-Francois, Castet Nicolas, and Henrion Jérôme. “SAR Imaging Challenges on UAV Trajectory Restitution Study Case with SAR-Light Prototype at X-Band”. In: *2022 IEEE International Symposium on Inertial Sensors and Systems (INERTIAL)*. 2022 IEEE International Symposium on Inertial Sensors and Systems (INERTIAL). May 2022, pp. 1–3. DOI: `10.1109/INERTIAL53425.2022.9787523`. URL: `https://ieeexplore.ieee.org/document/9787523` (visited on 04/09/2024).

[7] Xiaoyu Yan et al. “A Light-Weight SAR System for Multi-Rotor UAV Platform Using LFM Quasi-CW Waveform”. In: *2016 IEEE International Geoscience and Remote Sensing Symposium (IGARSS)*. 2016 IEEE International Geoscience and Remote Sensing Symposium (IGARSS). July 2016, pp. 7346–7349. DOI: `10.1109/IGARSS.2016.7730916`. URL: `https://ieeexplore.ieee.org/document/7730916` (visited on 04/09/2024).

[8] Giancarmine Fasano et al. “Proof of Concept of Micro-UAV-based Radar Imaging”. In: *2017 International Conference on Unmanned Aircraft Systems (ICUAS)*. 2017 International Conference on Unmanned Aircraft Systems (ICUAS). June 2017, pp. 1316–1323. DOI: `10.1109/ICUAS.2017.7991432`. URL: `https://ieeexplore.ieee.org/document/7991432` (visited on 05/17/2024).

[9] Mohamed-Amine Lahmeri et al. “Trajectory and Resource Optimization for UAV Synthetic Aperture Radar”. In: *2022 IEEE Globecom Workshops (GC Wkshps)*. 2022 IEEE Globecom Workshops (GC Wkshps). Rio de Janeiro, Brazil: IEEE, Dec. 4, 2022, pp. 897–903. ISBN: 978-1-66545-975-4. DOI: `10.1109/GCWkshps56602.2022.10008658`. URL: `https://ieeexplore.ieee.org/document/10008658/` (visited on 05/23/2024).

[10] Stephan Dill et al. “A Drone Carried Multichannel Synthetic Aperture Radar for Advanced Buried Object Detection”. In: *2019 IEEE Radar Conference (RadarConf)*. 2019 IEEE Radar Conference (RadarConf). Apr. 2019, pp. 1–6. DOI: `10.1109/RADAR.2019.8835814`. URL: `https://ieeexplore.ieee.org/document/8835814` (visited on 05/23/2024).

[11] Othmar Frey, Charles L. Werner, and Roberto Coscione. “Car-Borne and UAV-borne Mobile Mapping of Surface Displacements with a Compact Repeat-Pass Interferometric SAR System at L-band”. In: *IGARSS 2019 - 2019 IEEE International Geoscience and Remote Sensing Symposium*. IGARSS 2019 - 2019 IEEE International Geoscience and Remote Sensing Symposium. July 2019, pp. 274–277. DOI: `10.1109/IGARSS.`

2019.8897827. URL: https://ieeexplore.ieee.org/document/8897827 (visited on 04/09/2024).

[12] Bernd Arendt et al. “Influence of Vegetation on the Detection of Shallowly Buried Objects with a UAV-Based GPSAR”. In: *IGARSS 2022 - 2022 IEEE International Geoscience and Remote Sensing Symposium.* IGARSS 2022 - 2022 IEEE International Geoscience and Remote Sensing Symposium. July 2022, pp. 100–103. DOI: 10.1109/IGARSS46834.2022.9883635. URL: https://ieeexplore.ieee.org/document/9883635 (visited on 05/23/2024).

[13] Mehrdad Soumekh. *Synthetic Aperture Radar Signal Processing with MATLAB Algorithms.*

[14] Alexander Grathwohl et al. “Taking a Look Beneath the Surface: Multicopter UAV-Based Ground-Penetrating Imaging Radars”. In: *IEEE Microwave Magazine* 23.10 (Oct. 2022), pp. 32–46. ISSN: 1557-9581. DOI: 10.1109/MMM.2022.3188126. URL: https://ieeexplore.ieee.org/document/9878299 (visited on 04/08/2024).

[15] A. Freeman. “SAR Calibration: An Overview”. In: *IEEE Transactions on Geoscience and Remote Sensing* 30.6 (Nov. 1992), pp. 1107–1121. ISSN: 1558-0644. DOI: 10.1109/36.193786. URL: https://ieeexplore.ieee.org/document/193786 (visited on 04/09/2024).

[16] Bjoern Doering and Marco Schwerdt. “Introducing Equivalent Radar Cross Section - A First Step Toward New Radiometric Requirement Definitions”. In: EUSAR 2014; 10th European Conference on Synthetic Aperture Radar. June 2014, pp. 1–4. URL: https://ieeexplore.ieee.org/document/6857057 (visited on 05/18/2024).

[17] Kaijun Wu et al. “A New Drone-Borne GPR for Soil Moisture Mapping”. In: *Remote Sensing of Environment* 235 (Dec. 15, 2019), p. 111456. ISSN: 0034-4257. DOI: 10.1016/j.rse.2019.111456. URL: https://www.sciencedirect.com/science/article/pii/S0034425719304754 (visited on 04/09/2024).

[18] S. Pilia et al. “Airborne Multi-Frequency Microwave Radiometric Measurements in Synergy with SAR Data for the Retrieval of Soil Moisture”. In: *2020 16th Specialist Meeting on Microwave Radiometry and Remote Sensing for the Environment (MicroRad).* 2020 16th Specialist Meeting on Microwave Radiometry and Remote Sensing for the Environment (MicroRad). Nov. 2020, pp. 1–4. DOI: 10.1109/MicroRad49612.2020.9342544. URL: https://ieeexplore.ieee.org/document/9342544 (visited on 04/10/2024).

[19] Andreas Reigber et al. “Very-High-Resolution Airborne Synthetic Aperture Radar Imaging: Signal Processing and Applications”. In: *Proceedings of the IEEE* 101.3 (Mar. 2013), pp. 759–783. ISSN: 0018-9219, 1558-2256. DOI: `10.1109/JPROC.2012.2220511`. URL: `http://ieeexplore.ieee.org/document/6355595/` (visited on 05/22/2024).

[20] Arsenios Tsokas et al. “SAR Data Applications in Earth Observation: An Overview”. In: *Expert Systems with Applications* 205 (Nov. 1, 2022), p. 117342. ISSN: 0957-4174. DOI: `10.1016/j.eswa.2022.117342`. URL: `https://www.sciencedirect.com/science/article/pii/S0957417422006960` (visited on 05/17/2024).

[21] J. Ford et al. “Seasat Views North America, the Caribbean, and Western Europe with Imaging Radar”. In: Nov. 1, 1980. URL: `https://www.semanticscholar.org/paper/Seasat-views-North-America%2C-the-Caribbean%2C-and-with-Ford-Blom/1f69a3cf7db366bfbec2a05d30f1e90ecc8a3fa1` (visited on 04/11/2024).

[22] Wang Yang et al. “Internal and External Calibration of POLINSAR”. In: *Proceedings of 2011 IEEE CIE International Conference on Radar*. Proceedings of 2011 IEEE CIE International Conference on Radar. Vol. 1. Oct. 2011, pp. 879–882. DOI: `10.1109/CIE-Radar.2011.6159681`. URL: `https://ieeexplore.ieee.org/document/6159681` (visited on 05/28/2024).

[23] M. Younis et al. “Investigations on the Internal Calibration of Multi-Channel SAR”. In: *2017 IEEE International Geoscience and Remote Sensing Symposium (IGARSS)*. 2017 IEEE International Geoscience and Remote Sensing Symposium (IGARSS). July 2017, pp. 5386–5389. DOI: `10.1109/IGARSS.2017.8128221`. URL: `https://ieeexplore.ieee.org/document/8128221` (visited on 05/28/2024).

[24] Fan Feng et al. “Internal Calibration and Range Replica Extraction Scheme for Ultrahigh Resolution Spaceborne SAR”. In: *2019 6th Asia-Pacific Conference on Synthetic Aperture Radar (APSAR)*. 2019 6th Asia-Pacific Conference on Synthetic Aperture Radar (APSAR). Nov. 2019, pp. 1–4. DOI: `10.1109/APSAR46974.2019.9048533`. URL: `https://ieeexplore.ieee.org/document/9048533` (visited on 05/28/2024).

[25] Marc Jäger, Rolf Scheiber, and Andreas Reigber. “Robust, Model-Based External Calibration of Multi-Channel Airborne SAR Sensors Using Range Compressed Raw Data”. In: *Remote Sensing* 11.22 (22 Jan. 2019), p. 2674. ISSN: 2072-4292. DOI: `10.3390/`

rs11222674. URL: `https://www.mdpi.com/2072-4292/11/22/2674` (visited on 04/11/2024).

[26] P. Marques. “High Resolution SAR Imaging and Signal Processing”. In: 2016.

[27] Margaret Cheney and Brett Borden. *Fundamentals of Radar Imaging*. Society for Industrial and Applied Mathematics, 2009. DOI: `10.1137/1.9780898719291`. URL: `https://epubs.siam.org/doi/abs/10.1137/1.9780898719291`.

[28] Ludmilla Kolokolova et al. “Effects of Interaction of Electromagnetic Waves in Complex Particles”. In: *Electromagnetic Waves*. IntechOpen, June 21, 2011. ISBN: 978-953-307-304-0. DOI: `10.5772/16456`. URL: `https://www.intechopen.com/chapters/16081` (visited on 05/19/2024).

[29] Sophocles J. Orfanidis. *Electromagnetic Waves and Antennas*. Rutgers University, 2016. URL: `https://eceweb1.rutgers.edu/~orfanidi/ewa/`.

[30] Mark A. Richards. “Doppler Shift, Spatial Doppler, and the Stop-and-Hop Approximation for a Constant-Velocity Target”. In: (2010).

[31] Constantine A. Balanis. *Antenna Theory: Analysis and Design*. Third edition.

[32] Martin Štumpf. *Electromagnetic Reciprocity in Antenna Theory*.

[33] R.M. Mersereau and A.V. Oppenheim. “Digital Reconstruction of Multidimensional Signals from Their Projections”. In: *Proceedings of the IEEE* 62.10 (Oct. 1974), pp. 1319–1338. ISSN: 1558-2256. DOI: `10.1109/PROC.1974.9625`. URL: `https://ieeexplore.ieee.org/document/1451555` (visited on 05/17/2024).

[34] D.C. Munson, J.D. O’Brien, and W.K. Jenkins. “A Tomographic Formulation of Spotlight-Mode Synthetic Aperture Radar”. In: *Proceedings of the IEEE* 71.8 (Aug. 1983), pp. 917–925. ISSN: 1558-2256. DOI: `10.1109/PROC.1983.12698`. URL: `https://ieeexplore.ieee.org/document/1456966` (visited on 04/23/2024).

[35] M.D. Desai and W.K. Jenkins. “Convolution Backprojection Image Reconstruction for Spotlight Mode Synthetic Aperture Radar”. In: *IEEE Transactions on Image Processing* 1.4 (Oct. 1992), pp. 505–517. ISSN: 1941-0042. DOI: `10.1109/83.199920`. URL: `https://ieeexplore.ieee.org/document/199920` (visited on 04/23/2024).

[36] *NumPy Documentation — NumPy v1.26 Manual*. URL: `https://numpy.org/doc/stable/` (visited on 04/28/2024).

[37] *Kronecker Delta*. In: *Wikipedia*. Dec. 29, 2023. URL: `https://en.wikipedia.org/w/index.php?title=Kronecker_delta&oldid=1192529815` (visited on 04/29/2024).

[38] Nicholas Rahardiyan Rypkema. *A Straightforward Derivation of the Matched Filter*. Apr. 3, 2019. DOI: `10.31219/osf.io/gsjx3`. URL: `https://osf.io/gsjx3` (visited on 05/17/2024). preprint.

[39] Marc Jäger, Andreas Reigber, and Rolf Scheiber. "Accurate Consideration of Sensor Parameters in the Calibration and Focusing of F-SAR Data". In: *EUSAR 2012; 9th European Conference on Synthetic Aperture Radar*. EUSAR 2012; 9th European Conference on Synthetic Aperture Radar. Apr. 2012, pp. 20–23. URL: `https://ieeexplore.ieee.org/document/6216925` (visited on 04/05/2024).

[40] A. Reigber et al. "System Status and Calibration of the F-SAR Airborne SAR Instrument". In: *2011 IEEE International Geoscience and Remote Sensing Symposium*. 2011 IEEE International Geoscience and Remote Sensing Symposium. July 2011, pp. 1520–1523. DOI: `10.1109/IGARSS.2011.6049357`. URL: `https://ieeexplore.ieee.org/document/6049357` (visited on 04/05/2024).